

3D INVERSION OF MARINE MAGNETOTELLURIC DATA FROM SANTOS
BASIN

Paula Lima Ribeiro

Dissertação apresentada ao Programa de Pós-graduação em Geofísica do Observatório Nacional, como parte dos requisitos necessários à obtenção do título de Mestre em Geofísica.

Orientador(a): Dr. Sergio Luiz Fontes


Rio de Janeiro
Agosto - 2019

"3D INVERSION OF MARINE MAGNETOTELLURIC DATA FROM SANTOS
BASIN"

PAULA LIMA RIBEIRO

DISSERTAÇÃO SUBMETIDA AO CORPO DOCENTE DO PROGRAMA DE
PÓS-GRADUAÇÃO EM GEOFÍSICA DO OBSERVATÓRIO NACIONAL COMO
PARTE DOS REQUISITOS NECESSÁRIOS PARA A OBTENÇÃO DO GRAU
DE MESTRE EM GEOFÍSICA.

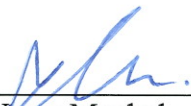
Aprovada por:



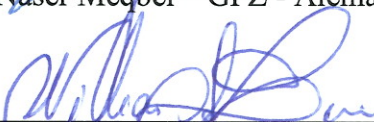
Dr. Sergio Luiz Fontes – ON/MCTIC
(Orientador)



Dr. Emanuele Francesco La Terra – ON/MCTIC



Dr. Naser Meqbel – GFZ - Alemanha



Dr. Williams Lima – ON/MCTIC

RIO DE JANEIRO – BRASIL

27 DE AGOSTO DE 2019

Lima Ribeiro, Paula

3D inversion of marine magnetotelluric data from Santos Basin/Paula Lima Ribeiro. – Rio de Janeiro: ON, 2019.

67 p., il.; 29, 7cm. Orientador(a): Sergio Luiz Fontes

Dissertação (mestrado) – ON/Programa de Pós-graduação em Geofísica, 2019.

Bibliography: p. 51 – 57.

1. magnetotelluric. 2. 3D inversion. 3. Santos Basin. I. , . II. Observatório Nacional, Programa de Pós-graduação em Geofísica. III. Título.

*The beginning of knowledge is
the discovery of something we do
not understand. (Frank Herbert)*

Acknowledgements

The completion of this work could not have been possible without the participation of so many people.

I would like to express my deep gratitude to my research advisor Sergio Fontes for his patient guidance, for his motivational talkings encouraging me in keeping my progress, for clarifying my doubts and providing me with all the tools that I needed.

I would also like to express my very great appreciation to Emanuele La Terra, Marcelo Banik, Ved Maurya and Naser Meqbel for their constructive suggestions and their willingness to give their time at all moments that I asked for it.

Assistance provided by Antonio França, José Antonio, Graça Brito, Thiago Moeda and Ronaldo Carvalho is greatly appreciated.

My special thanks are extended to Clarisse Fernandes, Flora Solon, Leonardo Miquelutti, Liliane Panetto, Nina Rocha, Vinicius Pinto, my colleagues from room 107 for sharing their experiences helping to solve my tasks.

I wish to acknowledge the financial support provided by CAPES, the structure and environment provided by Observatório Nacional and the teachers that I have the opportunity to learn from, the well log data provided by ANP and Petrobrás for funded the MT acquisition.

I specially thank all my family and friends. I don't even need to cite names but they know the importance of them at all steps of this work. Thank you for giving me all support (either emotional, financial, physically) that I needed to complete this journey as a better human than when I started. I have no words to express my gratitude to you.

Resumo da Dissertação apresentada ao Programa de Pós-Graduação em Geofísica do Observatório Nacional como parte dos requisitos necessários para a obtenção do título de Mestre em Geofísica.

3D INVERSION OF MARINE MAGNETOTELLURIC DATA FROM SANTOS BASIN

Paula Lima Ribeiro

Agosto/2019

Uma extensa campanha magnetotelúrica marinha (MMT) pioneira foi realizada na Bacia de Santos no Brasil em 2007 com o objetivo de avaliar a resposta do método em diferentes lâminas d'água em área de ocorrência de camada sedimentar pré-sal. Um total de 90 estações estão dispostas em 3 perfis com cerca de 250 km de extensão total. Os dados foram registrados no intervalo entre 10^{-1} a 10^4 s e apresentam boa qualidade. A análise de dimensionalidade, usando diferentes ferramentas, indica a forte influência de estruturas 3D nos dados MMT. A inversão 3D foi realizada com um código cuja minimização utiliza o método gradiente conjugado não linear de estrutura mínima (ModEM). A discretização da malha foi definida por 95 x 78 x 100 células e 1579 km x 1546 km x 696 km de tamanho nas direções x, y e z, respectivamente. Semi-espacos homogêneos com diferentes valores de resistividade foram testados como modelos iniciais, assim como diferentes valores do parâmetro de regularização inicial para a inversão. O meio-espaço homogêneo de 10 Ω .m e o valor de 10 para o parâmetro de regularização inicial foram selecionados como melhores parâmetros. A avaliação do modelo foi feita baseada nos valores do erro médio quadrático e uma comparação entre os valores de resistividade obtidos na inversão e o dado de indução de poço disponível. Um bom ajuste foi encontrado entre eles. Finalmente, correlacionamos a inversão com uma interpretação sísmica. A presença do embasamento é muito clara na porção noroeste do perfil central e uma feição vertical relativamente resistiva na porção sudeste pode ser indicativa do diapirismo salino.

Abstract of the Dissertation presented to the National Observatory's Graduate Program in Geophysics as a partial fulfillment of the requirements for the degree of Master in Geophysics.

3D INVERSION OF MARINE MAGNETOTELLURIC DATA FROM SANTOS BASIN

Paula Lima Ribeiro

August/2019

A large pioneer marine magnetotelluric (MMT) campaign were made at the Santos Basin in Brazil in 2007 aiming to asses the outcome of the method in a wide range of water depths in region where pre-salt sediments are present. A total of 90 sites are displaced along three profiles of about 250 km of total. Good data quality from 10^{-1} to 10^4 s were recorded. Dimensionality analysis using different tools indicates the strong influence of 3D structures in the MMT data. 3D inversion was carried out using a code with minimization performed by a minimum structure non-linear conjugate gradient inversion scheme (ModEM). The grid discretization was defined by 95 x 78 x 100 cells and 1579 km x 1546 km x 696 km of size in x , y and z directions respectively. Homogeneous half-spaces with different background resistivities were tested as initial models as well as different values of the initial regularization parameter for the inversion. The 10 Ω .m homogeneous half-space and the value of 10 for the starting regularization parameter were selected as the optimal choices. The model assessment was made based on the normalized root mean square (nRMS) values and a comparison between the values of resistivity resulted from inversion and an available induction log data. A good fit were found between them. Finally, we correlated the inversion result with a seismic based interpretation. The basement is very clear in the northwest portion of the central profile and a vertical relative resistive feature in the southeast portion can be indicative of the salt diapirism.

Contents

List of Figures	ix
List of Tables	xii
1 Introduction	1
2 Objectives	2
3 Regional Setting	3
3.1 Brazilian Continental Margin	3
3.1.1 The Divergent Margin	3
3.2 Santos Basin	4
3.2.1 Tectonic and stratigraphic evolution	4
3.2.2 Petroleum Systems	9
4 Theory of Magnetotellurics	12
4.1 MT Frequency Range	12
4.2 MT Signal Sources	13
4.3 Skin Depth	13
4.4 Basic Physics	14
4.5 Marine Magnetotelluric Method	18
5 MT Data Treatment	20
5.1 Processing	20
5.2 Dimensionality Analysis	20
5.2.1 Rotational Invariants of the Impedance Tensor	21
5.2.2 Phase Tensor	22
5.3 3D MT Inversion	23
5.3.1 ModEM	27
6 The Magnetotelluric Data from Santos Basin	29
6.1 Dimensionality Analysis	30
6.2 Data Preparation	30

6.3 Mesh Design	32
6.4 Initial models	33
6.5 Inversion Parameters	33
6.6 Results of the 3D Inversion	33
6.6.1 Low resistive unit	40
6.6.2 Intermediate resistive unit	40
6.6.3 High resistive unit	40
6.7 Comparison with previous results	43
6.8 Interpretation	45
7 Conclusions	49
Bibliography	51
Appendix	58

List of Figures

3.1	Sketch of the evolutionary model of the divergent Brazilian continental margin. The description of each evolutionary phase (a), (b), (c), (d) and (e) can be found in the text. (Source: CAINELLI and MOHRIAK (1999))	5
3.2	Location of the MMT sites in the Santos Basin with background bathymetry. Gray polygon delimits the salt area.	6
3.3	Stratigraphic column of Santos Basin. (Source: MOREIRA <i>et al.</i> (2007))	11
4.1	The power spectrum of natural magnetic variations. Interactions in the Earth-ionosphere waveguide generate high frequency signals, while low frequency signals are generated by solar wind-magnetosphere. The zoom box shows the minimization of signal amplitude around 1 s known as MT dead-band (Source: Simpson & Bahr, 2005).	14
4.2	Graphic of the skin depth in function of period considering homogeneous half-space with different electrical resistivities background: 0.3 Ω .m, 1 Ω .m, 10 Ω .m, 50 Ω .m, 100 Ω .m and 1000 Ω .m.	15
4.3	Sketch of a seafloor equipment (Source: Constable <i>et al.</i> , 1998).	19
5.1	Table showing the dimensionality criteria proposed by Weaver <i>et al.</i> , 2000 (Source: Martí <i>et al.</i> , 2009).	22
5.2	Graphic representation of the phase tensor (Source: Caldwell <i>et al.</i> , 2004).	23
6.1	Dimensionality analysis of geoelectric structures by period of each station for the three profiles using the WALDIM code (Martí <i>et al.</i> , 2009).	30
6.2	Dimensionality analysis of geoelectric structures by period of each station for the three profiles employing the skew angle β of the phase tensor. This image was generated using the MTPy package (Krieger & Peacock, 2014).	31

6.3	Sections from the 3D final models for all profiles using the initial model of 10 Ω .m for initial λ values of: (a)1; (b) 10; and (c) 100. The lateral profiles have stations only in the distance from 20 to 80 km approximately. The white rectangles in it indicate the part of the profiles must be neglected.	35
6.4	Sections from the 3D final models for all profiles using the initial model of 50 Ω .m for initial λ values of: (a)1; (b) 10; and (c) 100. The lateral profiles have stations only in the distance from 20 to 80 km approximately. The white rectangles in it indicate the part of the profiles must be neglected.	36
6.5	Graphic of nRMS values versus number of iterations for: (a) the initial model of 10 Ω .m and different initial λ values; and (b) the initial model of 50 Ω .m and different initial λ values.	37
6.6	Normalized root mean square (nRMS) misfit for the full impedance tensor at each site in all three profiles obtained by inversion with the six different inversion tests carried out.	37
6.7	Apparent resistivity and phase curves for the stations L24E_79, L24E_91, L24_11, L24_45, L24W_61 and L24W_76. The dots represents the observed data an the line represents the predicted data obtained by inversion with the initial model of 10 Ω .m and initial λ values of: (a)1; (b) 10; and (c) 100.	38
6.8	Apparent resistivity and phase curves for the stations L24E_79, L24E_91, L24_11, L24_45, L24W_61 and L24W_76. The dots represents the observed data an the line represents the predicted data obtained by inversion with the initial model of 50 Ω .m and initial λ values of: (a)1; (b) 10; and (c) 100.	39
6.9	Comparison between resistivity log from well sps42 and resistivity values derived from the MMT inversion tests along site L24_45 at the same location. The thick black line represents the preferred model result at the well log location. Right image is a lithology column from the sps42 borehole. The resistivity and lithology information of the well sps42 were obtained from the Petroleum National Agency (ANP).	41

6.10 (a) Vertical sections from the 3D final model along the three profiles using the initial model of 10 Ω .m for initial λ value of 10, chosen as our preferred model (as in Figure 6.3b), with labels of the main geoelectrical units. The gray dashed lines separate a low, an intermediate and a high resistive zone. C1 and C2 identify the pronounced conductors; R1, R2 and R3 the resistors; and the question mark the relatively resistive vertical feature delineated by a filled black line. The lateral profiles have stations only in the distance from 20 to 80 km approximately. The white rectangles in it indicate the part of the profiles must be neglected. (b) Maximum depth of penetration for xy and yx directions of each site estimated from the Niblett-Bostick depth approximation.	42
6.11 Depth slices from our preferred final model. The black line delineates the coast line and the orange color represents the seawater.	44
6.12 NW-SE section of the electrical resistivity model obtained from a separate 2D magnetotelluric inversion based on SMITH and BOOKER (1991) approach. (Source: GALLARDO <i>et al.</i> (2012))	45
6.13 (a) Geospectral image of joint inversion overlain by a migrated seismic section (FONTES <i>et al.</i> , 2009). Resistivity, seismic slowness and density are illustrated in RGB and magnetization in contours spaced every 0.2 Amp/m. (b) Table illustrating the annotated zones and corresponding property ranges in the image above. The colors in the geospectral column match those represented in (a) whereas the magnitude of vectors represent the magnetization contrast. (Source: GALLARDO <i>et al.</i> (2012))	46
6.14 Section from the 3D preferred final models for the central profile with contour lines added.	47
6.15 Geological interpretation based on a seismic line located at the same position of the MMT central profile. The MMT sites are drawn in the ocean seafloor. (Source: DE LUGAO <i>et al.</i> (2008))	47

List of Tables

5.1 Comparison of forward modelling approaches.	25
5.2 Comparison of inversion algorithms (Modified from Siripuaraporn, 2012).	27
6.1 Summary of the number of iterations and final nRMS value obtained after run the inversion with the different combinations of initial models and λ values. The subindex 0 indicates the initial value of nRMS.	34

Chapter 1

Introduction

Santos Basin is considered a basin with a high potential for oil production and still presents areas to be better explored. The presence of promising reservoirs associated with pre-salt layers leads to the formation of complex structures which can be challenging for subsurface imaging. Recently, the technological development allowed the application of electromagnetic methods in marine environments (CONSTABLE *et al.*, 1998).

The initial incredibility of the use of the magnetotelluric method in the ocean at significant depths was due to the known attenuation of the electromagnetic signals in seawater (CHAVE *et al.*, 1991). Over the past two decades, the development of better acquisition equipments and data processing and inversion algorithms has allowed the application and a major acceptance of the marine magnetotelluric method (MMT). As an example, one of the largest marine MT surveys was conducted in Gemini Prospect in the Gulf of Mexico, aiming to demonstrate that the salt's base can be mapped using MMT.

In Brazil, one of the largest MMT campaigns was carried out in the Santos Basin. Previous works (FONTES *et al.* (2009) and GALLARDO *et al.* (2012)) obtained good results applying two-dimensional (2D) inversion. Therefore, we believe that it is possible to improve the results with an application of 3D inversion methodology.

This dissertation is organized as follows: chapter 2 presents the research objectives; in chapter 3, we briefly describe the regional geology of the study area; the basic fundamentals of the magnetotelluric method are introduced in chapter 4, chapter 5 discusses MT data treatment, chapter 6 discourses about application of this treatment to the MMT from Santos Basin discussing the 3D inversion results and, finally, chapter 7 presents the conclusions.

Chapter 2

Objectives

Recently, the use of electromagnetic methods in petroleum exploration has earned a great relevance, being employed as an efficient tool in the subsurface imaging, mainly, in environments where seismic reflection methods present limitations. The magnetotelluric method is one of the techniques that has gained greater reliability, but the interpretation of its data still needs improvements.

Numerical inversion plays an important role to obtain a reasonable interpretation of geophysical data. The inversion of MT data historically started with 1D cases and in the 70s the 2D inversion was already applied. In the last decades, considerable improvements in the instrumentation and in the acquisition techniques and advances in the development of numerical methods and computational performance contributed to the evolution of the 3D inversion (EGBERT *et al.*, 2017). Currently, 3D inversion codes have become available and more accessible, resulting in more reliable 3D MT models produced by the scientific community.

The main goal of this research is to achieve a geoelectrical model of the region with better quality and resolution by applying 3D inversion. Therefore, with this improvement, we expect to cooperate with the greater valorization of the marine magnetotelluric method use in the oil exploration and to asses its effectiveness.

Chapter 3

Regional Setting

3.1 Brazilian Continental Margin

The Brazilian continental margin was formed resulting from the Gondwana supercontinent breakup (Late Jurassic - Early Cretaceous). The rupture and the plates motion caused the separation of the African and South American continents and emergence of the South Atlantic ocean. The occurrence of different tectonic efforts and depositional environments, added to the local climate, provided the different sedimentation patterns and structures present in the current Brazilian sedimentary basins.

Several evolutionary models seek to explain the genesis and development of these basins (e.g. [ASMUS and BAISCH \(1983\)](#); [CHANG *et al.* \(1992\)](#)). Currently, the most accepted model is the one proposed by [MCKENZIE \(1978\)](#). Based on tectono-physical concepts, the author proposed the combination of two processes as a cause of the evolution of the sedimentary basins: (i) lithospheric stretching with consequent thinning of the lithosphere and (ii) thermal subsidence associated to the cooling of the thermal anomaly of the asthenosphere.

Based on the different types of relative movement of tectonic plates, the Brazilian continental margin is divided into three parts. The transforming segment encompasses from the Foz do Amazonas Basin to the Potiguar Basin and this portion is known as the Equatorial Margin. The transversal segment comprises the Pernambuco-Paraíba, Sergipe-Alagoas and Jacuípe Basins, called the Northeast Margin. The divergent segment, known as the East, Southeast and South Margin, which covers the Camamu to Pelotas Basins, in which the Santos Basin is located (study area of the present work).

3.1.1 The Divergent Margin

[CAINELLI and MOHRIAK \(1999\)](#) defined five main phases of the geodynamic evo-

lution of the Divergent Margin of the South Atlantic Ocean based on the characterization of tectonics and sedimentation (Figure 3.1).

The first phase started with the extension processes that moved the South American and African continents apart. At that time, there was a slight uplift of the asthenosphere and thinning of the continental crust and upper mantle. Thin sedimentary layers were deposited along the spaces left by the faults formed in the crust (Figure 3.1-a).

In the following phase, a greater stretch of the lithospheric portion occurred along with a magmatic extrusion. A higher number of faults was established, allowing the formation of semi-graben structures, where lacustrine continental sediments were deposited (Figure 3.1-b).

The end of the rifting process marked the third phase, characterized by an increase in the lithospheric stretching that inclined the faults and sedimentary layers formed previously (Figure 3.1-c).

The fourth phase is defined by the beginning of the formation of oceanic crust. Major faults were reactivated. The occurrence of continental and oceanic magmatism and blocks of the rift section were eroded, marking a separation between continental and marine depositional environments (Figure 3.1-d).

In the last phase, the carbonate deposits were gradually replaced by the sedimentation of the deep water, with later uplift of the Serra do Mar, which led to siliciclastic sedimentation (Figure 3.1-e).

3.2 Santos Basin

The Santos marine basin is a basin of passive margin located on the east coast of Brazil, more precisely, in front of the states of Rio de Janeiro, São Paulo, Paraná and Santa Catarina (Figure 3.2). It is confined between the Campos and Pelotas basins, being bounded by the Cabo Frio High to the north, Florianópolis High to the south, the Plateau of São Paulo to the east and by the belts of coastal mountains to the west.

It extends for about 1200 km of the Brazilian coast and covers a totally immersed area of approximately 350,000 km². The thickness of the seawater varies from 400 to 3000 m. It is among the most extensive sedimentary basins in Brazil and presents a significant petroleum potential.

3.2.1 Tectonic and stratigraphic evolution

In the 1970s, the first stratigraphic chart of the Santos Basin was defined. With the advancement of the region's studies, due to the growth of exploratory interest, it

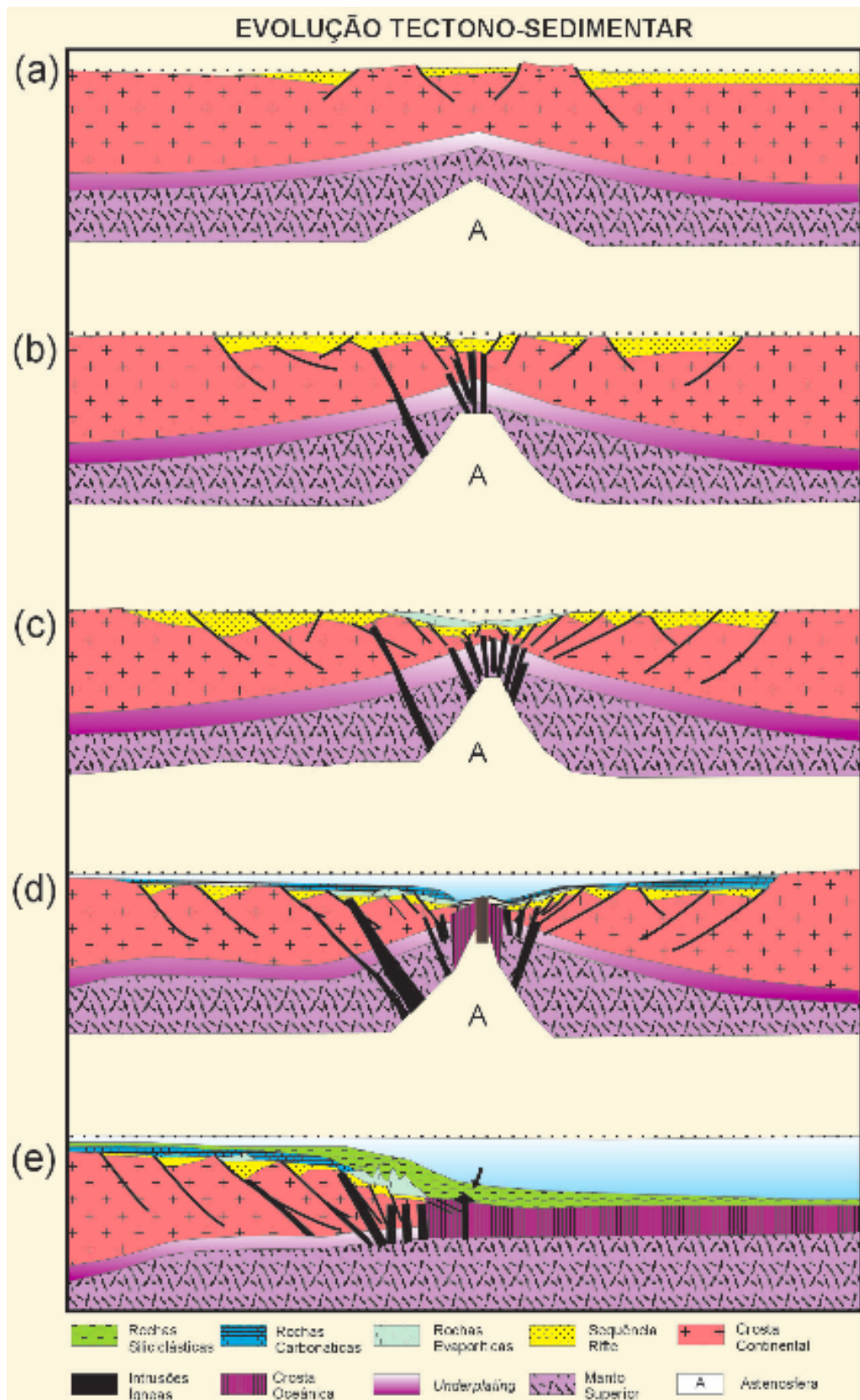


Figure 3.1: Sketch of the evolutionary model of the divergent Brazilian continental margin. The description of each evolutionary phase (a), (b), (c), (d) and (e) can be found in the text. (Source: [CAINELLI and MOHRIAK \(1999\)](#))

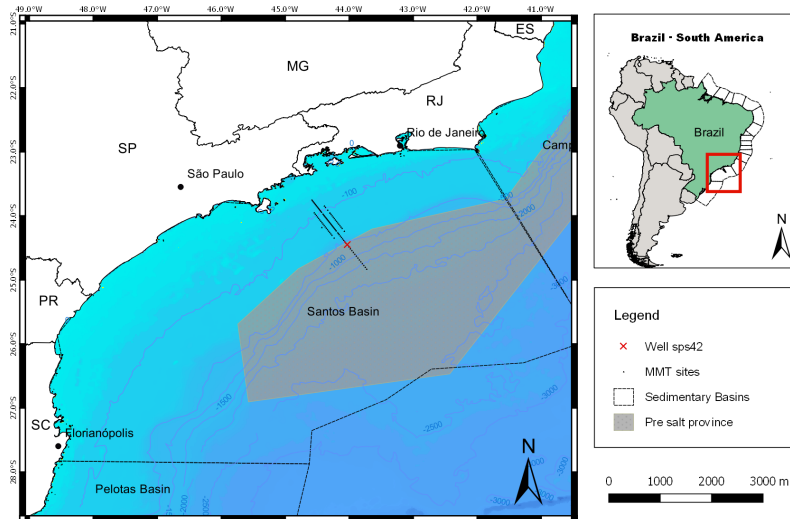


Figure 3.2: Location of the MMT sites in the Santos Basin with background bathymetry. Gray polygon delimits the salt area.

has been complemented and was most recently updated by MOREIRA *et al.* (2007). The author divided the basin into four main lithostratigraphic groups: Guaratiba, Camburi, Frade and Itamambuca, which are overlying the crystalline basement of the Santos Basin defined by pre-Cambrian granites and gneisses of the Ribeira Belt (Fig: 3.3). According to MOREIRA *et al.* (2007), there are also three main phases of the tectonic evolution of the Santos Basin: Rift, Post-Rift and Drift, which comprise these groups.

The sedimentary formations are described below based on the stratigraphic column of the Santos Basin referred to (MOREIRA *et al.*, 2007).

I - Guaratiba Group

The Guaratiba Group consists of five formations: Camboriú, Piçarras, Itapema, Barra Velha and Ariri, of which the first three belong to the rift phase and the last two, to the post-rift phase. Its sedimentary record occurs from the Hautevirian and extends to the beginning of the Albian.

Camboriú Formation

The Camboriú Formation is the first sedimentary record of the Santos Basin. It is characterized by basaltic flows from Cretaceous. There is a possible correlation of this formation with the formations Cambiúnas of the Campos Basin and Ibituba of the Pelotas Basin. It has a lower limit discordant with the rocks of the basement and upper limit discordant with the sediments of the Piçarras formation.

Piçarras Formation

The Piçarras Formation is formed by alluvial fans of conglomerates and sandstones in the proximal facies and by sandstones, siltstones and shales in lacustrine environments. Its sediments were deposited in the Barremian. It has lower limit discordant with the top of the basalts of the Camboriú Formation and in its upper limit the discordance of the base of the Itapema Formation.

Itapema Formation

The Itapema Formation is composed of alluvial fans of conglomerates and sandstones in the proximal portions and calcirrudite interspersed with dark shales in the distal portions. Its sediments were deposited from the Neobarremian to the Eoaptian. Its upper limit is the pre-Alagoas discordance.

Barra Velha Formation

The Barra Velha Formation is characterized by the transition from continental depositional environment to shallow marine. It presents alluvial fans of sandstones and conglomerates in the proximal portions and intercalations of limestones and shales in the distal portions. Its sedimentary deposition occurred during the Aptian. Its lower limit is given by pre-Alagoas discordance and its upper limit is the basis of evaporites.

Ariri Formation

The Ariri Formation is formed by evaporites, which extend to the north of the Pelotas Basin. They were deposited in Neoaptian. It has equivalents in the basins of Campos (Retiro Member), Espírito Santo (Itaúnas Formation), Camamu-Almada (Igrapiúna Formation) and Sergipe (Ibura Formation).

II - Camburi Group

It begins the Drift phase, in which the Camburi Group encompasses the sediments deposited from the alluvial fans to the pelite and sandstones of the bathyal region that were deposited after the Ariri Formation to the top of the Cenomanian, representing a transgressive phase. In this group, the Florianópolis, Guarujá and Itanhaém formations are present.

Florianópolis Formation

The Florianópolis Formation, from Albian to Cenomanian age, comprises conglomerates, sandstones and shales from the proximal portions that were deposited in

alluvial and delta fans systems. There are equivalent alluvial fans in other basins, such as the Goitacás Member in Campos and the Tramandaí Formation in the Pelotas Basin.

Guarujá Formation

The carbonate platform implanted during the Eoalbian corresponds to the Guarujá Formation. It is characterized by shales, calcilutites, calcirrudites, calcarenites and marls. It is possible to correlate with the Quissamã Member (Campos Basin) and the Porto Belo Formation (Pelotas Basin), for example.

Itanhaém Formation

The Itanhaém Formation occurs as shales and marls. Its correlation is attributed to Atlântida Formation of Pelotas Basin and to the Outeiros Member of Campos Basin.

III - Frade Group

The Frade Group is composed of all sediments deposited from the top of the Cenomanian to the Cretaceous/Paleogene boundary. This unit represents a regression phase. It is divided by the Santos, Juréia and Itajaí-Açu formations.

Santos Formation

The Santos Formation is marked by conglomerates and sandstones intercalated with shales and clays of proximal facies.

Juréia Formation

The Juréia Formation is represented by sandstones, shales and siltstones that were deposited from continental environment to proximal regions of the platform. It has related units in other basins such as the formations Cidreira of the Pelotas Basin and the Emborê of the Campos Basin.

Itajaí-Açu Formation

The Itajaí-Açu Formation is composed of shales and argillites deposited in the environments of distal platform, slope and basin. There are dispersed turbiditic sandstones that were denominated Ilha Bela Member. It is correlated with the Tamoios Member (Campos Basin) and the Imbé Formation (Pelotas Basin).

IV - Itamambuca Group

The Itamambuca Group encompasses the sediments deposited from the Paleocene to the present day. It is composed of the Ponta Aguda, Iguape, Marambaia and Sepetiba formations.

Ponta Aguda Formation

The Ponta Aguda Formation presents conglomerates and sandstones deposited in an environment of alluvial fans, fluvial systems and coastal deposits with intercalation of mud.

Iguape Formation

The Iguape Formation is characterized by calcarenites and calcilutites intercalated with argillites, siltstones and marls. It was deposited in a carbonate platform environment.

Marambaia Fomation

Shales, marls, diamictites and intercalated sandstones compose the Marambaia Formation deposited in the regions of distal platform, slope and basin.

Sepetiba Formation

The Sepetiba Formation is identified by sandstones, coquinas, molluscs, bryozoans and foraminifera corresponding to the environment of coastal fans.

3.2.2 Petroleum Systems

The petroleum systems of the Santos Basin and its main models of hydrocarbon accumulation are reported by [CHANG *et al.* \(2008\)](#). The two oil systems in the basin are: Guaratiba-Guarujá and Itajaí-Açu-Ilhabela. Since, in [MOREIRA *et al.* \(2007\)](#), the old Guaratiba Formation was elevated to the category of group and Ilhabela is the denomination of a member, we will treat here the referred petroleum systems as Piçarras and Itajaí-Açu respectively.

In general, the Piçarras Formation is considered as the main hydrocarbon generating rock of the basin. Migration occurs through faults, salt windows and permeable layers that facilitate the movement of hydrocarbons (carrier-beds). Shales, intraformational calcilutites, and the thick layer of evaporites act as a seal. Most of the traps are structural or mixed, with great predominance of traps generated by the halokinesis.

Piçarras System

The source rocks of the Piçarras System are laminated black shales intercalated with carbonates with a thickness of 100 to 300 meters. They were deposited in lacustrine saline environment at the end of the rift phase. It present high to excellent generative potential with average values of Total Organic Carbon (TOC) between 2 and 6 % and the presence of kerogen type I.

The reservoirs of this system are carbonates of the formations Itapema (coquinas) and Barra Velha (microbialites), which belong to the Guaratiba Group, and the Guarujá Formation (oolitic calcarenites). The occurrence of facies with different concentrations of granulometry leads to a variety of porosity values (low to high). Siliciclastic reservoirs also occur, such as the turbidite sandstones of Ilhabela member and sandstones of the Santos/Juréia Formation with mean porosity values of 12 %.

The evaporites of the Ariri Formation are excellent seals for the carbonate reservoirs, as well as the calcilutites and pelites of the Itanhaém Formation. For siliciclastic reservoirs, the pelites of the Itajaí-Açu, Santos/Juréia and Marambaia formations act as sealing rocks.

Itajaí-Açu System

The source rocks of the Itajaí-Açu System are shales deposited in an anoxic marine environment with organic matter types II and III with a mean concentration of TOC of 1 %, with some peaks of 6 %. They are in the early stages of thermal maturity.

Only the siliciclastic rocks act as reservoirs of this system, having the pelites of the formations Itajaí-Açu, Santos/Juréia and Marambaia, intercalated with the sandstones, playing the role of seal.

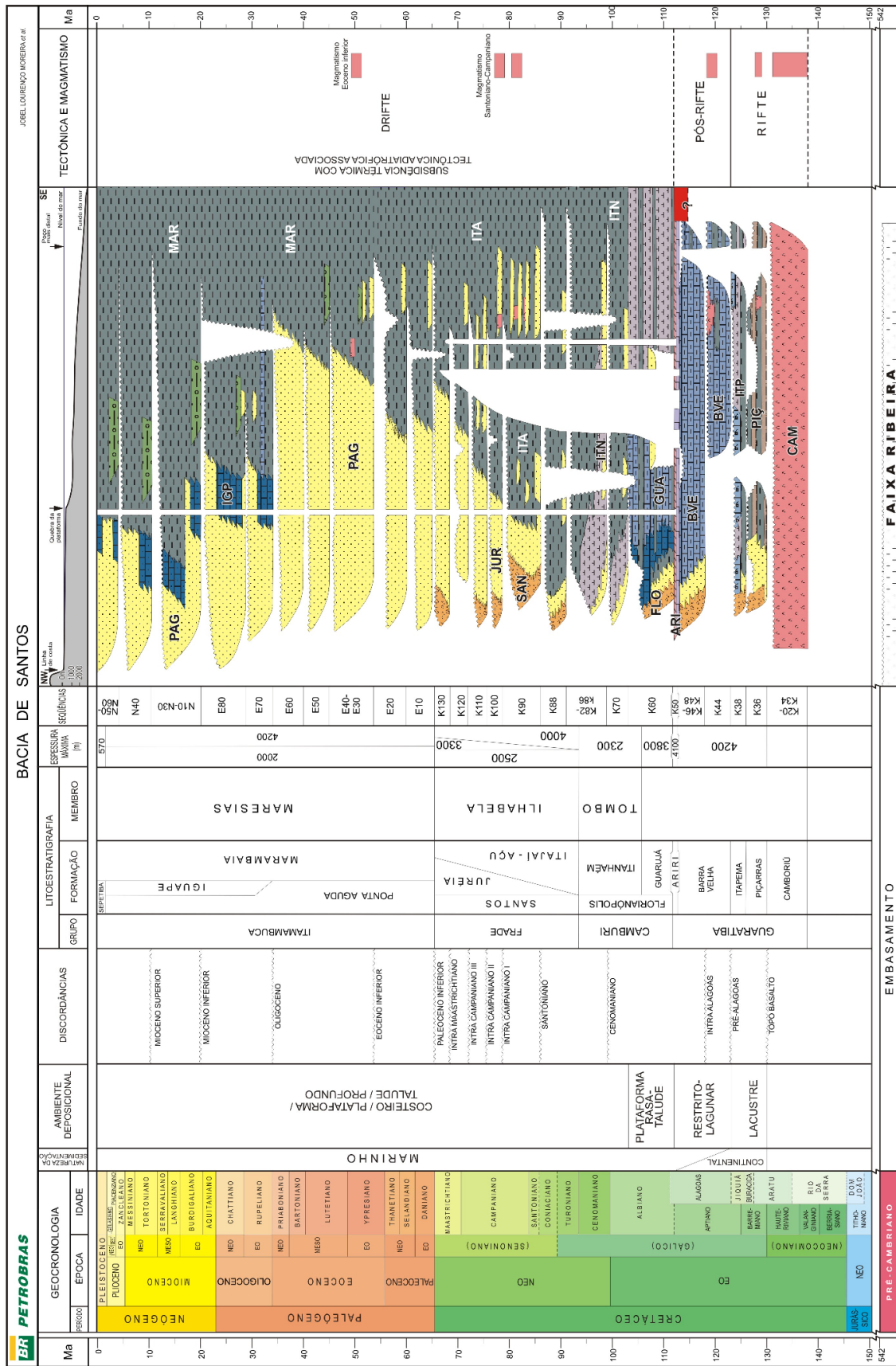


Figure 3.3: Stratigraphic column of Santos Basin. (Source: MOREIRA *et al.* (2007))

Chapter 4

Theory of Magnetotellurics

The Magnetotelluric (MT) method is a non-invasive geophysical technique that allows estimating the distribution of electrical conductivity of the Earth's subsurface by measuring time variations of the Earth's natural electromagnetic (EM) field. RIKITAKE (1948), TIKHONOV (1950) and CAGNIARD (1953) were the first to present the theoretical fundamentals of the method independently. They noted that measurements of the electric and magnetic field fluctuations could be used to derive complex ratios between these fields which would describe the penetration of electromagnetic fields in Earth.

The method is based on the principle of electromagnetic induction. EM waves are generated by physical phenomena within the Earth's atmosphere and magnetosphere impinging on the Earth's surface. Most of this signal is reflected back into the atmosphere and a small part is transmitted into the Earth. Then, electric currents are induced in the ground, generating a secondary electromagnetic field. The components of magnetic (B_x , B_y and B_z) and electric (E_x and E_y) fields in orthogonal directions are measured at the surface of the Earth by using coils and non-polarizable electrodes respectively. By treating these measurements, the variation of the electrical resistivity in function of depth is estimated.

4.1 MT Frequency Range

The natural oscillations of the Earth's magnetic field extend over a broad frequency range (around 10^{-15} to 10^6 Hz). The minor frequency fluctuations (approximately 10^{-11} Hz) are observed in paleomagnetic studies, while magnetotelluric studies traditionally use frequency band ranging from 10^{-5} to 10^4 Hz. This wide frequency range allows the method to image a broad span of depths, being useful in a variety of applications, from shallow crustal to deeper mantle studies.

Based on the frequency range used in data acquisition, magnetotelluric equipment can be classified as: (i) Long-period MT (LMT) - measures variations from

10^{-4} to 1 Hz, reaching depths of hundreds of kilometers; (ii) Broadband MT (BBMT) - records data in a frequency band of 10^{-3} to 10^3 Hz; and (iii) audiomagnetotelluric (AMT) - between 10 Hz and 10 kHz, reaching depths of tens of meters to 15 km.

Additionally, the instruments also can be classified based on the source of the signals: (i) Controlled-source AMT (CSAMT) - uses an artificial source to create EM signals and operates from 10^{-1} to 10^4 Hz; and (ii) Radio MT (RMT) - uses EM signals transmitted by remote station of radio with frequency ranging from 10^4 to 10^6 Hz and depth of investigation from 1 to 100 m.

4.2 MT Signal Sources

The natural EM signals have their sources coming from different regions from the core of the Earth to distant galaxies (VOZOFF, 1991). In particular, the MT signal sources are generated by two different processes dependent on frequency. Signals with a frequency higher than 1 Hz (short period signals) are generated in low Earth's atmosphere due to worldwide electrical storms that occurs mainly in equatorial zones, while low-frequency signals (less than 1 Hz) are originated in magnetosphere where an interaction occurs between the geomagnetic field and solar winds.

VOZOFF (1991) classified the use of natural sources by MT as being at the same time a great advantage and disadvantage of the method. This fact is advantageous considering other research methods because it has a lower cost and easier logistics, since there is no need of artificial sources. However, EM signals of natural origin can not be fully controlled. Around 1 Hz and 1 kHz, the electromagnetic signal has low intensity, known as MT dead-bands (Figure 4.1). Therefore, the acquired data may present poor quality in this frequency range. One way to get around these effects is by using an artificial signal source (CSAMT).

4.3 Skin Depth

A quite widespread and important concept in EM methods is the skin depth. Skin depth is defined as the depth of investigation where the amplitude of the electromagnetic signal decays by a factor of $1/e$ (inverse of Euler's number) of its surface value. This attenuation is directly related to the electrical resistivity of the medium and inversely to the frequency used. It can be calculated by:

$$\delta = \sqrt{\frac{2}{\omega\mu\sigma}} = 503\sqrt{\frac{\rho}{f}} = 503\sqrt{\rho T} \text{ (m)}, \quad (4.1)$$

where ω is the angular frequency (rad/s), μ is the magnetic permeability (H/m)

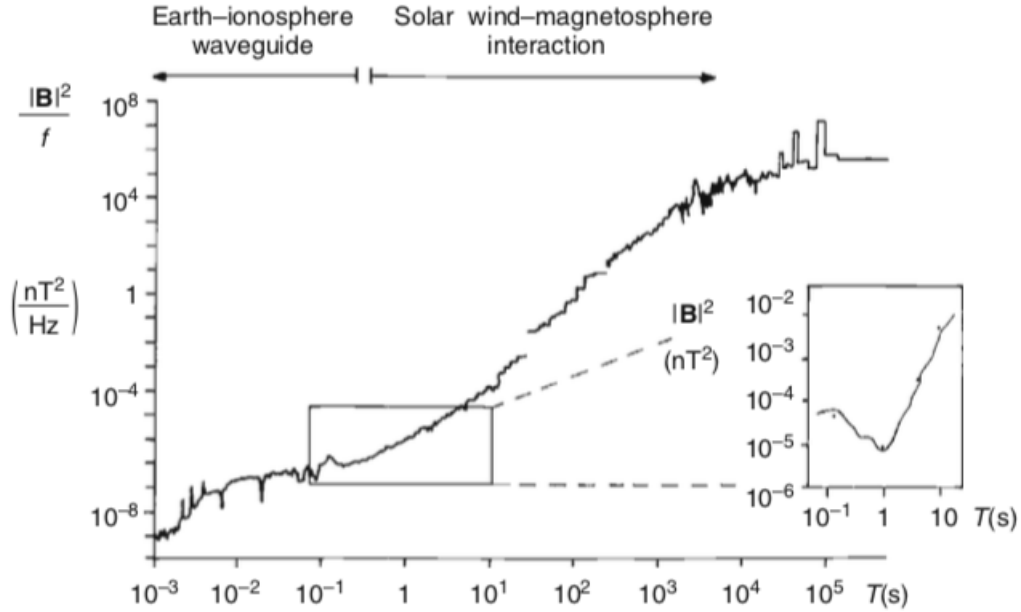


Figure 4.1: The power spectrum of natural magnetic variations. Interactions in the Earth-ionosphere waveguide generate high frequency signals, while low frequency signals are generated by solar wind-magnetosphere. The zoom box shows the minimization of signal amplitude around 1 s known as MT dead-band (Source: Simpson & Bahr, 2005).

(considered as the free-space value $\mu_0 = 4 \pi \times 10^{-7}$ H/m), σ is the electric conductivity (S/m) of the medium, its reciprocal ρ is the electrical resistivity ($\Omega \cdot \text{m}$) of the medium, f is the linear frequency (Hz) and T is the period (s).

Figure 4.2 illustrates the skin depth for different homogeneous half-spaces in the period range of 10^{-2} to 10^4 s. It is notable that conductive environments need the use of low frequency (long periods) to penetrate deeper compared to more resistive environments.

4.4 Basic Physics

The magnetotelluric method is based on electromagnetic phenomena that are governed by the Maxwell's equations expressed, in differential form, by

$$\nabla \times \mathbf{E} = -\frac{\partial \mathbf{B}}{\partial t} \quad (4.2)$$

$$\nabla \times \mathbf{H} = \mathbf{J} + \frac{\partial \mathbf{D}}{\partial t} \quad (4.3)$$

$$\nabla \cdot \mathbf{D} = \eta \quad (4.4)$$

$$\nabla \cdot \mathbf{B} = 0 \quad (4.5)$$

in that \mathbf{E} and \mathbf{H} are the electric (V/m) and magnetic field vectors (A/m), \mathbf{B} is the magnetic induction vector (T or W/m²), \mathbf{D} is the dielectric displacement vector

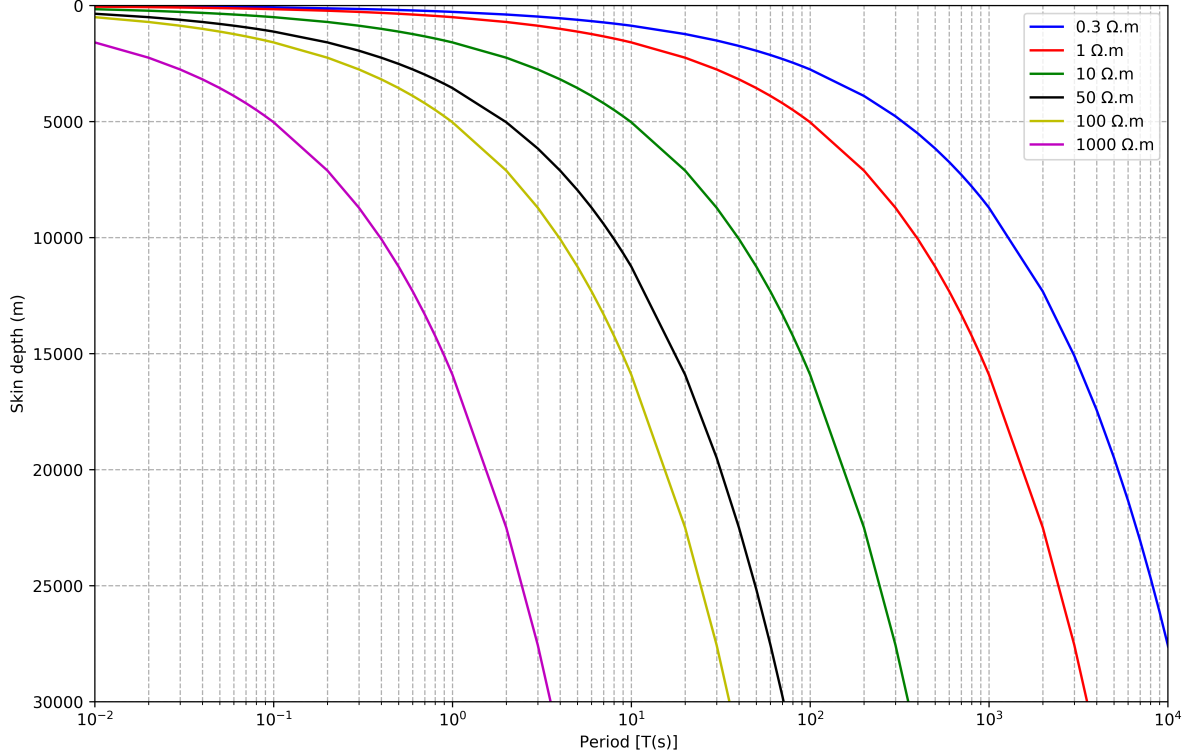


Figure 4.2: Graphic of the skin depth in function of period considering homogeneous half-space with different electrical resistivities background: 0.3 $\Omega\cdot\text{m}$, 1 $\Omega\cdot\text{m}$, 10 $\Omega\cdot\text{m}$, 50 $\Omega\cdot\text{m}$, 100 $\Omega\cdot\text{m}$ and 1000 $\Omega\cdot\text{m}$.

(C/m^2), \mathbf{J} is the electric current density vector (A/m^2) and η is the volumetric density of electric charge (C/m^3).

Equation (4.2) is the Faraday's Law and states that time-varying magnetic field induces an electrical field. Equation (4.3) corresponds to Ampère-Maxwell's law and states that a magnetic field can be generated by the movement of charges varying in time being directly proportional to the current flow. Equation (4.4) is called Gauss's law for electricity, which affirms that electric charges are sources of electric field flux. Gauss' law for magnetism (Equation 4.5) affirms that no monopoles exist.

Because of the low intensities of the natural electromagnetic fields, these equations can be related to the constitutive relations, which are given by

$$\mathbf{D} = \epsilon\mathbf{E} \quad (4.6)$$

$$\mathbf{B} = \mu\mathbf{H} \quad (4.7)$$

$$\mathbf{J} = \sigma\mathbf{E}, \quad (4.8)$$

where ϵ , μ and σ represent electrical permittivity (F/m), magnetic permeability (H/m) and electrical conductivity (S/m) respectively and are parameters describing intrinsic properties of the material in which the electromagnetic wave propagates. These equations are valid for an isotropic environment under linearity conditions.

In anisotropic cases, these parameters would be expressed in a tensor form. The equation (4.8) is known as Ohm's Law.

For the Earth study, in this work, it is considered that: (i) the subsurface medium behaves as an isotropic medium; (ii) there is a linearity condition; (iii) the electrical properties of the medium do not vary with time, temperature and pressure; and (iv) the magnetic permeability μ and the electric permittivity ϵ assume their respective values in a vacuum, i.e., $\mu = \mu_0 = 4\pi \times 10^{-7}$ H/m and $\epsilon = \epsilon_0 \approx 8.85 \times 10^{-12}$ F/m.

Assuming a plane wave with amplitude at the surface E_0 , a harmonic temporal dependence in the form of $e^{i\omega t}$ and using the constitutive relations and assumptions above, the equations (4.2) to (4.5) become

$$\nabla \times \mathbf{E} + i\omega\mathbf{B} = 0 \quad (4.9)$$

$$\nabla \times \mathbf{B} - \mu_0(\sigma + i\omega\epsilon_0)\mathbf{E} = 0 \quad (4.10)$$

$$\nabla \cdot \epsilon_0\mathbf{E} = \rho \quad (4.11)$$

$$\nabla \cdot \mathbf{B} = 0. \quad (4.12)$$

Applying mathematical manipulations and considering a homogeneous medium free of electromagnetic sources $\nabla \cdot \mathbf{E} = \nabla \cdot \mathbf{H} = 0$, the Helmholtz equations in \mathbf{E} e \mathbf{B} are given by

$$\nabla^2\mathbf{E} + \kappa^2\mathbf{E} = 0 \quad (4.13)$$

$$\nabla^2\mathbf{B} + \kappa^2\mathbf{B} = 0, \quad (4.14)$$

in which $\kappa = \sqrt{\omega^2\mu_0\epsilon_0 - i\omega\mu_0\sigma} = \sqrt{-\hat{z}\hat{y}}$ is known as wave number, $\hat{z} = i\omega\mu_0$ is defined as impeditivity and $\hat{y} = \sigma + i\omega\epsilon_0$, admittivity of the medium.

The frequency used in the MT probes varies from 10^{-3} to 10^4 Hz and the conductivities in the terrestrial subsurface are generally between 10^{-6} and 10 S/m. Thus, the displacement currents $\mathbf{J}_d = \partial\mathbf{D}/\partial t = i\omega\epsilon_0\mathbf{E}$ are neglected compared to driving currents $\mathbf{J} = \sigma\mathbf{E}$, that is,

$$\frac{|\mathbf{J}_d|}{|\mathbf{J}|} = \frac{\omega\epsilon_0}{\sigma} \ll 1, \quad (4.15)$$

that is, $\sigma \gg \omega\epsilon_0$. Thus, we have that $\kappa^2 = \omega^2\mu_0\epsilon_0 - i\omega\mu_0\sigma \approx -i\omega\mu_0\sigma$ and the equations (4.13) and (4.14) become

$$\nabla^2\mathbf{E} - i\omega\mu_0\sigma\mathbf{E} = 0 \quad (4.16)$$

$$\nabla^2\mathbf{B} - i\omega\mu_0\sigma\mathbf{B} = 0, \quad (4.17)$$

which are the diffusion equations of the electromagnetic fields.

In a uniform half-space, for the one-dimensional (1D) case, we obtain as solution of the equation (4.16):

$$E_x = Ae^{-\kappa z} + Be^{+\kappa z}, \quad (4.18)$$

where A and B are constants and z refers to the vertical depth. Since the electric field must decrease with depth increasing, this solution becomes:

$$E_x = Ae^{-\kappa z}. \quad (4.19)$$

Thus, from equation (4.9), we can obtain:

$$B_y = \frac{\kappa i}{\omega} E_x \text{ or } H_y = \frac{\kappa i}{\omega \mu_0} E_x. \quad (4.20)$$

The ratio between the orthogonal components of the electric and magnetic fields is defined as impedance and is given by:

$$Z_{xy}(\omega) = \frac{E_x}{H_y} = \frac{-i\omega\mu_0}{\kappa}. \quad (4.21)$$

From this, apparent resistivity is derived:

$$\rho_a = \frac{|Z_{xy}(\omega)|^2}{\omega\mu_0} \quad (4.22)$$

and phase:

$$\phi = \arctan \left[\frac{\Im(Z(\omega))}{\Re(Z(\omega))} \right]. \quad (4.23)$$

In the general case, the relationship between the horizontal components of the electric and magnetic fields can be written as:

$$\begin{bmatrix} E_x(\omega) \\ E_y(\omega) \end{bmatrix} = \begin{bmatrix} Z_{xx}(\omega) & Z_{xy}(\omega) \\ Z_{yx}(\omega) & Z_{yy}(\omega) \end{bmatrix} \begin{bmatrix} H_x(\omega) \\ H_y(\omega) \end{bmatrix} \quad (4.24)$$

or in the tensorial form:

$$\mathbf{E}_h = \bar{\mathbf{Z}}\mathbf{H}_h \quad (4.25)$$

where the subindices h indicates horizontal components.

The relation between the vertical and horizontal components of the field \mathbf{H} can also be expressed in terms of a complex vertical transfer function or tipper \mathbf{T} given

by

$$H_z(\omega) = \begin{bmatrix} T_{xz}(\omega) & T_{yz}(\omega) \end{bmatrix} \begin{bmatrix} H_x(\omega) \\ H_y(\omega) \end{bmatrix} \quad (4.26)$$

or

$$H_z = \mathbf{TH}_h. \quad (4.27)$$

It can be used as a dimensionality indicator and detection of conductors.

A more detailed description can be found in SIMPSON and BAHR (2005).

4.5 Marine Magnetotelluric Method

Traditionally, the magnetotelluric method has been applied on land. Its first applications on offshore environment were used for mantle tectonic studies (as in FILLOUX (1980); OLDENBURG (1981); KELLETT *et al.* (1991); MATSUNO *et al.* (2010)) using receivers composed by fluxgate magnetometers and DC-coupled electric sensors measuring MT fields in a frequency band ranging from 10^{-5} to 10^{-3} Hz.

To conduct crustal studies or to employ the marine magnetotelluric (MMT) method for petroleum exploration, it is necessary to record data at higher frequencies. However, the MT dead-band (around 1 Hz) added to the fact that the conductance of seawater attenuates significantly the EM signal makes the MMT application for oil prospect not feasible. Having that in mind, CONSTABLE *et al.* (1998) developed a seafloor instrumentation with AC-coupled sensors, induction coils, and electric field amplifier that are sensitive in the range of 10^{-3} to 1 Hz, making viable crustal studies and petroleum exploration by employing the MMT method.

A MMT survey consists in the deployment of the receivers on the ocean floor from a vessel with a defined spacing. Each receiver includes a 150 kg anchor to hold it to the seafloor, an acoustic unit with a release mechanism that allows to unattach the instrument from the anchor and a positioning mechanism to track the equipment position, and a flotation system that allows the receiver to be recovery back to the surface by means of its own buoyancy. The Ag-Ag chloride electrodes are at the end of two 10 m lengths polypropylene pipes forming the electric dipoles and the magnetometer sensors are composed by aluminum wire coils. A drawing of a seafloor instrument is showed in Figure 4.3. Generally, the recording period lasts about 2 or 3 days and then the measured time series can be downloaded and observed .

Investigations applied to oil exploration can be seen in HOVERSTEN *et al.* (2000) and KEY *et al.* (2006). This application presents great relevance in situations

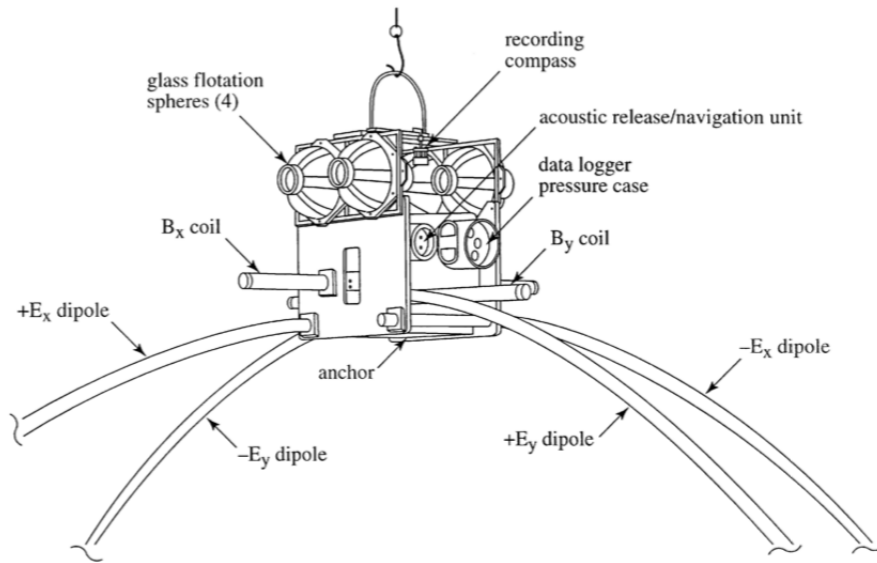


Figure 4.3: Sketch of a seafloor equipment (Source: Constable et al., 1998).

in which the seismic have low resolution imaging, as, for example, beneath salt, volcanics or carbonate layers.

Besides the acquisition, another important factor in the marine magnetotelluric method is the shape of the ocean floor. Bathymetry can have major distorting effects on the MT data and must be considered during the modelling and inversion.

Chapter 5

MT Data Treatment

Magnetotelluric data are recorded as continuous time series of each field component E_x , E_y , B_x , B_y and B_z . These time series undergo a visual analysis to remove eventual spikes that are caused by electromagnetic noise contaminating the MT signals. After that, a number of steps (described in sections 5.1, 5.2 and 5.3) are followed in order to derive the final geoelectric model.

5.1 Processing

MT time series are processed to yield frequency-domain estimates of the complex impedance tensor elements and the vertical transfer function (VTF). The apparent resistivity and phase are derived from the impedance values as explained in section 4.4. Currently, the most common processing schemes apply the Cascade Decimation Method (WIGHT *et al.*, 1977), a technique that computes Fast Fourier Transform, within a time series window, resulting in information in the frequency-domain. Next, the method of robust statistics is applied to average the multiple estimates of the impedance smoothing the spectral information obtained, as proposed by EGBERT and BOOKER (1986).

Another technique in use to improve the quality of the impedance results is the remote reference (GAMBLE *et al.*, 1979). MT data recorded simultaneously at different locations allows the use of one site less affected by noise (in special, coherent noise) as reference to remove biased measurements in the station of interest.

5.2 Dimensionality Analysis

Once the apparent resistivity and phase curves are obtained, before modelling and inverting MT data, it is important to define the data geoelectrical dimensionality. The aim is to determine if the electrical resistivity is varying only with one direc-

tion (1D or unidimensional data), two directions (2D or two-dimensional data) or three directions (3D or tridimensional data). In the real world, we can visualize these 3 situations in different geological environments. Within a sedimentary basin, for example, we can characterize a stratified layered earth, in which the electrical resistivity varies only with depth, resulting to 1D data. In a situation where two homogeneous blocks are separated by a vertical fault, the resistivity varies with the two horizontal directions, thus, the data is classified as 2D. 3D data is common in complex geological structures such as in the presence of a salt dome, where the resistivity varies along all directions.

Depending on the data dimensionality, the elements of the impedance tensor $\bar{\bar{\mathbf{Z}}}(\omega)$, in equation 4.24, have particular values. For the 1D case, $Z_{xx} = Z_{yy} = 0$ and $Z_{xy} = -Z_{yx}$ and the impedance tensor $\bar{\bar{\mathbf{Z}}}(\omega)$ becomes

$$\bar{\bar{\mathbf{Z}}}(\omega) = \begin{bmatrix} 0 & Z_{xy}(\omega) \\ -Z_{xy}(\omega) & 0 \end{bmatrix}. \quad (5.1)$$

For the 2D case, the subsurface resistivity varies in two directions. The direction in which the electrical resistivity of a 2D medium does not change is called the geoelectric strike. In this case, having the axis x parallel to the direction of the geoelectric strike, the matrix is represented by

$$\bar{\bar{\mathbf{Z}}}(\omega) = \begin{bmatrix} 0 & Z_{xy}(\omega) \\ Z_{yx}(\omega) & 0 \end{bmatrix}. \quad (5.2)$$

For the three-dimensional case, the resistivity varies in all directions and none of the elements of the tensor impedance is null.

Currently, several tools are available to assess the dimensionality of the MT data: Swift skew (SWIFT, 1967), Bahr skew (BAHR, 1988), ellipticity (WORD *et al.*, 1970), polar diagrams, Groom-Bailey dimensional analysis (GROOM and BAILEY, 1989), rotational invariants of the impedance tensor (WEAVER *et al.*, 2000) and phase tensor (CALDWELL *et al.* (2004); BIBBY *et al.* (2005)).

In this work, the presence of complex geological structures in the study area (associated with pre-salt play) itself characterizes the physical properties of the region with a three-dimensional character. However, to evaluate quantitatively the dimensionality of the MMT data, the two more recent tools cited above were used: the rotational invariants of the impedance tensor and the skew angle of the phase tensor.

5.2.1 Rotational Invariants of the Impedance Tensor

WEAVER *et al.* (2000) suggests the characterization of geoelectric dimensionality

based on the rotational invariants of the MT tensor $\mathbf{M}(\omega)$, known as WAL invariant. The MT tensor is defined by the ratio between the electric and magnetic induction fields, that is

$$M_{ij}(\omega) = \frac{E_i}{B_j} = \frac{1}{\mu_0} Z_{ij}(\omega) \quad (5.3)$$

with $i,j=x,y$ or

$$\bar{\mathbf{M}}(\omega) = \frac{1}{\mu_0} \bar{\mathbf{Z}}(\omega). \quad (5.4)$$

The rotational invariants are scalar values derived from the observed MT tensor that do not depend on the orientation of the axes in which the data were measured (its computation is described in WEAVER *et al.* (2000)). These eight invariants can be represented in a Mohr circle diagram and interpreted in terms of geoelectric dimensionality as show in Figure 5.1.

Case	I_3 to I_7 and Q values	Geoelectric dimensionality
1	$I_3 = I_4 = I_5 = I_6 = 0$	1D $\rho_{1D} = \mu_0((R_1^2 + R_2^2)/\omega)$, $\varphi_{1D} = \arctan(I_2/I_1)$
2	$I_3 \neq 0$ or $I_4 \neq 0$; $I_5 = I_6 = 0$; $I_7 = 0$ or $Q = 0$ ($\xi_4 \neq 0$ and $\eta_4 \neq 0$)	2D
3a	$I_3 \neq 0$ or $I_4 \neq 0$; $I_5 \neq 0$; $I_6 = 0$; $I_7 = 0$	3D/2D twist 2D affected by galvanic distortion (only twist)
3b	$I_3 \neq 0$ or $I_4 \neq 0$; $I_5 \neq 0$; $I_6 = 0$; $Q = 0$	3D/1D 2D Galvanic distortion over a 1D or 2D structure (non-recoverable strike direction)
3c	$I_3 \neq 0$ or $I_4 \neq 0$; $I_5 = I_6 = 0$; $I_7 = 0$ or $Q = 0$ ($\xi_4 = 0$ and $\eta_4 = 0$)	3D/1D 2D diag Galvanic distortion over a 1D or 2D structure resulting in a diagonal MT tensor
4	$I_3 \neq 0$ or $I_4 \neq 0$; $I_5 \neq 0$; $I_6 \neq 0$; $I_7 = 0$	3D/2D General case of galvanic distortion over a 2D structure
5	$I_7 \neq 0$	3D (affected or not by galvanic distortion)

Figure 5.1: Table showing the dimensionality criteria proposed by Weaver et al., 2000 (Source: Martí et al., 2009).

In this work, we used the WALDIM code provided by MARTI *et al.* (2009), based on the WAL invariants criteria, for the study of the dimensionality of MMT data.

5.2.2 Phase Tensor

The phase tensor Φ is defined as the ratio between the real and imaginary parts of the impedance tensor. Considering \mathbf{X} and \mathbf{Y} as the real and imaginary parts of the impedance tensor respectively, that is, $\mathbf{Z} = \mathbf{X} + i\mathbf{Y}$, thus the phase tensor is

$$\Phi = \mathbf{X}^{-1}\mathbf{Y} = \begin{pmatrix} \Phi_{xx} & \Phi_{xy} \\ \Phi_{yx} & \Phi_{yy} \end{pmatrix}. \quad (5.5)$$

The phase tensor is considered to be a good tool for dimensionality analysis because it is not affected by galvanic distortions (a phenomenon caused by the presence of 3D conductivity heterogeneities near the surface of the Earth).

CALDWELL *et al.* (2004) and BIBBY *et al.* (2005) demonstrate the use of this tool to determine the dimensionality of the MT data. It can be represented graphically as an ellipse, characterized by a semi-major axis Φ_{max} , a semi-minor axis Φ_{min} and the angle $\alpha - \beta$ between the reference coordinate system and the semi-major axis (Figure 5.2), where Φ_{max} , Φ_{min} and the skew angle β given by

$$\beta = \frac{1}{2} \arctan\left(\frac{\Phi_{xy} - \Phi_{yx}}{\Phi_{xx} + \Phi_{yy}}\right) \quad (5.6)$$

are the coordinate invariants that describe the phase tensor. In the 3D case, the skew angle β is non-zero and the ellipse is flattened, in a 2D case, β is zero and for 1D, the ellipse becomes a circle.

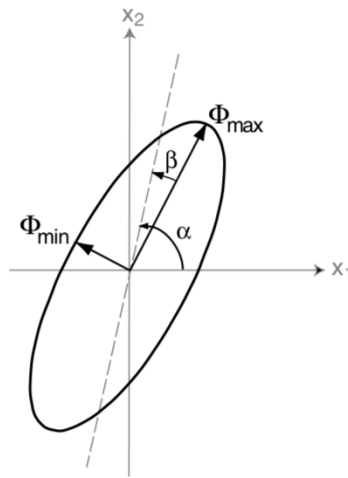


Figure 5.2: Graphic representation of the phase tensor (Source: Caldwell et al., 2004).

5.3 3D MT Inversion

Finally, to investigate the structures in subsurface, it is necessary to proceed to inversion of geophysical data. However, before to deal with an inverse problem, it is reasonable to address the forward problem since an inversion code is based on a forward solution.

A forward problem is defined by the process of predicting data given a hypothetical physical property model of the Earth considering a physical principle and specific conditions relevant to the problem. Mathematically, the model parameters m_j ($j=1, 2, \dots, M$) and the functions F_i ($i=1, 2, \dots, N$) that related the data to the model parameters are known and by applying the forward modelling it is possible to calculate the data d_i by

$$d_i = F_i(m_1, m_2, \dots, m_M) \text{ with } i = 1, 2, \dots, N \quad (5.7)$$

or

$$\mathbf{d} = F(\mathbf{m}) \quad (5.8)$$

where $F(\mathbf{m}) = (F_1(\mathbf{m}) F_2(\mathbf{m}) \dots F_N(\mathbf{m}))^T$ with T referring to the transposed matrix.

On the other hand, in the inverse problem, the model parameters m_j are unknown. So, the inversion aims to estimate models describing how a physical property is distributed in subsurface based on measurements of geophysical survey data. In the mathematical form, it consists in computing \mathbf{m} by finding the inverse of F (F^{-1}), that is

$$\mathbf{m} = F^{-1}(\mathbf{d}) \quad (5.9)$$

Equations 5.7, 5.8 and 5.9, however, describe an ideal situation where the inversion of F exists and the error \mathbf{e} between the observed and predicted data is zero. In the real world, generally the F^{-1} does not exist and there are errors associated to the modelling and to the experiment itself (cultural or instrument noise), leading to

$$\mathbf{d} = F(\mathbf{m}) + \mathbf{e}. \quad (5.10)$$

So, the inverse problem consists in solving Equation 5.10 for the unknown model parameters \mathbf{m} . Thus, the general idea is to find a model that produces responses that match the observed responses considering the errors.

It is important to have in mind that a variety of models can generate similar fits to the observed data - this is known as the non-uniqueness of the inverse problem. To circumvent it, it is important to constrain the model, considering all prior information available, and evaluate the results not only by the data fit, but also by the geological context in which the data is inserted.

Thus, solving the MT inverse problem means to estimate models of distribution of electrical resistivity on the basis of measurements of amplitude and phase or real and imaginary parts of the impedance tensor for a given frequency at each site by using the Maxwell equations. For this purpose, a set of mathematical techniques are included in the EM inverse theory that can be separated into three main elements: forward modelling, optimization and regularization.

In the forward modelling, to solve Maxwell's equations, two numerical methods have been proposed in the literature. In the integral equations (IE) method only the conductivity anomaly is discretized requiring less computational power but being limited to very simple geologic situations. Early publications (RAICHE (1974), 1975 Hohmann, WANNAMAKER (1991)) implements the IE solver in the conven-

tional way, but, more recently, other authors (AVDEEV *et al.* (1997), HURSAN and ZHDANOV (2002), ZHDANOV *et al.* (2006), KRUGLYAKOV and KUVSHINOV (2018)) have contributed to improve the technique by reformulating the approach and showing its efficiency. Nevertheless, in more complex and realist geological structures, the employment of the differential equation method (either finite differences (FD), finite elements (FE) or finite volume (FV)) has become more popular (REDDY *et al.* (1977), MACKIE *et al.* (1993), SIRIPUNVARAPORN *et al.* (2002), WEISS (2013), BELLO *et al.* (2019)) in EM forward codes. In the latter approach, not only the conductivity anomaly is discretized but also the structures surrounding it, demanding more storage space and computing time.

Table 5.1 shows the advantages and drawbacks of the most popular methods applied in 3D EM modelling in a general form. It is important to emphasize that another factors, besides the format of the system of equations, inside each forward code such as governing equation, formulation type, staggered grid, solver, pre conditioner and convergence correction also influences the accuracy and computation time of the algorithms. Variations of these terms are proposed by many authors as a way to overcome its issues and achieve more effective codes. The choice of the best suited algorithm for each problem might be done based on each specific problem.

Forward modelling	System of equations	Advantages	Disadvantages
IE method	Complex and dense but more compact than FD and FE	Less computational power than FD and FE	It is not well adequate to discretize very complex inhomogeneous structures
FD method	Complex, large, sparse and symmetric	Implementation is straightforward; Fast convergence	Difficult inclusion of topography and bathymetry compared to FE
FE method	Complex, large, sparse and non-symmetric	More accurate than IE and FD to discretize complex structures including topography and bathymetry	Hard to implement; Slow convergence

Table 5.1: Comparison of forward modelling approaches.

After the forward solution, the EM inversion aims to find a best-fitting model that minimizes a penalty (or objective) functional $\varphi(\mathbf{m})$ - a sum of data misfit (or data functional) $\varphi_d(\mathbf{m})$ and model norm terms (or model functional or stabilizing

functional) $\varphi_m(\mathbf{m})$ pondered by a trade-off parameter λ , that is, $\min_{\mathbf{m}, \lambda} \varphi(\mathbf{m}, \lambda)$, described by

$$\varphi(\mathbf{m}) = \varphi_d(\mathbf{m}) + \lambda\varphi_m(\mathbf{m}). \quad (5.11)$$

Considering the least-squares solution, the data misfit $\varphi_d(\mathbf{m})$ assumes a squared weighted L_2 -norm of the residual vector, that is $\mathbf{d} - F(\mathbf{m})$, thus

$$\varphi_d(\mathbf{m}) = (\mathbf{d} - F(\mathbf{m}))^T \mathbf{C}_d^{-1} (\mathbf{d} - F(\mathbf{m})) \quad (5.12)$$

where \mathbf{C}_d is a covariance matrix of data errors. Defining the stabilizing functional $\varphi_m(\mathbf{m})$ as the amount of spatial roughness in the model, that is

$$\varphi_m(\mathbf{m}) = (\mathbf{m} - \mathbf{m}_0)^T \mathbf{C}_m^{-1} (\mathbf{m} - \mathbf{m}_0) \quad (5.13)$$

with \mathbf{m}_0 being a prior or first guess model parameter and \mathbf{C}_m the model covariance or smoothing operator. Thus, the objective function described in Equation 5.11 can be rewritten as:

$$\varphi(\mathbf{m}, \mathbf{d}) = (\mathbf{d} - F(\mathbf{m}))^T \mathbf{C}_d^{-1} (\mathbf{d} - F(\mathbf{m})) + \lambda(\mathbf{m} - \mathbf{m}_0)^T \mathbf{C}_m^{-1} (\mathbf{m} - \mathbf{m}_0). \quad (5.14)$$

To sum up, the inverse algorithms search for an optimal model parameter by minimizing the data misfit constrained by the model roughness.

The solution of this optimization problem (Eq. 5.14) can be calculated by applying different schemes as proposed by distinct authors such as: Gauss-Newton (GN) - SASAKI (2004) and FARQUHARSON *et al.* (2002); Gauss-Newton with Conjugate Gradient (GN-CG) - MACKIE and MADDEN (1993) and SIRIPUNVARAPORN and EGBERT (2007); Quasi-Newton (QN) - NEWMAN and BOGGS (2004) and AVDEEV and AVDEEVA (2009); and Non-linear conjugate gradiente (NLCG) - RODI and MACKIE (2001) and COMMER and NEWMAN (2009). A comparison between them showing the main advantages and disadvantages of each method is shown in Table 5.2. A great review about the main algorithms of 3D electromagnetic inversion can be found in AVDEEV (2005) and SIRIPUNVARAPORN (2012).

Note (Eq. 5.14) that the regularization parameter λ controls the relative weight between the minimization of the data misfit and the stabilizing functional. Choosing large values of λ yields to heavily minimization of model roughness, producing smoother models.

For our research, the inversion was performed in the software ModEM (EGBERT and KELBERT (2012); KELBERT *et al.* (2014)) described below.

Inversion algorithm	Advantages	Disadvantages
GN method	Small number of iterations to converge	Large CPU time and memory usage; often impractical to apply; convergence depends on λ ; must use several values of λ
GN-CG method	Same as GN method but small amount of memory usage	Convergence depends on λ ; must use several values of λ ; can fail to converge for some λ ; can be slower than GN method
QN method	Small amount of memory usage	Convergence rate is slower than others
NLCG method	Small amount of memory usage	Convergence rate depends on λ , but comparable to GN; must run with several values of λ ; Can fail to converge for some λ

Table 5.2: Comparison of inversion algorithms (Modified from Siripuaraporn, 2012).

5.3.1 ModEM

EGBERT and KELBERT (2012) describes a general mathematical framework for frequency-domain EM geophysical inverse problems that provides a foundation for implementation of a Modular System for Electromagnetic Inversion referred as ModEM (a more detailed description of the software can be found in KELBERT *et al.* (2014)). ModEM was developed at Oregon State University and it is distributed for free for non-commercial academic use.

ModEM is a versatile algorithm that can be applied to a wide range of EM data types as well as allows the implementation of different model parametrization and regularization schemes. Here, we used ModEM to invert 3D magnetotelluric data with the non-linear conjugate gradient (NLCG) method applied to the non-quadratic objective functional (Eq. 5.14). The forward modelling is based on a 3D staggered-grid finite-difference (YEE, 1966), each cell is parameterized independently, and the regularization is built by means of the penalization of the deviations from a prior model with smoothness enforced using a model covariance. With the model covariance, it is possible to control the applied smoothing in all directions and also to fix some model parameter, as when we include topography or bathymetry, we fix the values of resistivity in the ocean and air cells.

The program is coded in Fortran 95 programming language, has a command-line

interface and its structure is organized into modules and dependencies. The three general levels are numerical discretization, interface and generic inversion. The basic data objects are the data (**d**), the model parameters (**m**) and the EM solution and source field vectors (**e** and **b**). This overall formulation allows easy modification for developers.

The large matrices and vectors involved in the forward modelling and inversion of 3D MT data requires an extensive memory space and computational time, making the code execution in common machines impracticable. Therefore, ModEM is implemented following a parallelization method over frequencies in a PC cluster using MPI (Message Passing Interface) communication mechanism as suggested by MEQBEL (2009).

In what concerns performing 3D inversion with ModEM, the user might be aware that all steps of data treatment are important to prevent misinterpretations of the results (as in all inverse problems). There is not a recipe to follow and consequently achieve success in the inversion, but some mistakes can be avoided. Checking the quality of the MT data removing biased points that can generate artifacts in the inversion, defining an adequate grid discretization, testing the inversion running with different initial models and parameters, placing the boundaries far away from the data profiles to avoid boundary effects, comparing results and being critical to analyze what the result stands for are some reminders to conduct a satisfactory inversion. For all this, it is important for the user to know the data that she/he is working with and to understand how the inversion program works.

Thereby, it is relevant to discuss how the inversion algorithm inside ModEM converges. There are options used as sufficient decrease condition and stopping criteria in the ModEM inversion code that can be defined by the user. The algorithm starts with an initial guess model introduced by the user; at each iteration this model is updated in the search of model parameters that generate a value of objective functional less than the previous one. The program will repeat this loop until reach a root mean square (RMS) misfit value less than a threshold or when the λ is less than a specific value or when it achieves a maximum number of iterations.

Another inversion parameter that can be controlled by the user is the regularization factor λ . In most of NLCG algorithms, λ remains with a fixed value, however, in ModEM, the λ starts with an initial value and is decreased by a factor of 10 at each iteration in which the difference between current and previous iteration data misfit is less than 0.002. This procedure is a way to ensure that the algorithm can scape from a local minimum without loss of orthogonality of the search direction vectors in the NLCG algorithm as mentioned by MEQBEL *et al.* (2016).

Chapter 6

The Magnetotelluric Data from Santos Basin

The marine magnetotelluric data were acquired in Santos Basin, at the north of Mexilhão field, by WesternGeco Electromagnetics in collaboration with Observatório Nacional/MCTIC and Petrobras in August 2007. A total of 90 sites composes three MMT profiles oriented in NW-SE direction (Figure 3.2). Among these stations, 56 make up the central profile of about 160 km in length, another 34 comprise two adjacent lateral profiles (16 in the eastern profile and 18 in the western profile) with an extension of approximately 55 km each. Another station is set apart these profiles working as a remote reference¹.

The spacing between stations varies from 2 km in the shallow part to 4 km in the deepest part. The water depth ranges from 72 to 1689 m. The data was acquired using a sampling rate of 62.5 Hz, obtaining data in a frequency range from 10 to 0.0003 Hz². The equipment used was produced by EMI - Electromagnetic Instruments Inc. and is known as MMT-24. The data was processed robustly using remote reference.

To obtain a reliable interpretation model, the inversion relies on a study of dimensionality, a good data preparation, an appropriate mesh design, an adequate initial model and an optimal choice of inversion parameters. These aspects are discussed in the following sections and, finally, the inversion results are shown.

¹In practice, two stations were used as remote reference: one for shallow part and the station that was used as remote reference of the deep part belongs to the central profile.

²The upper limit of this range varies along the central profile due to the attenuation of EM signal caused by the seawater. Sites located in deeper water usually spans from 1 to 0.0003 Hz.

6.1 Dimensionality Analysis

As discussed in Section 5.2, we used two tools to determine the data dimensionality. With the use of WALDIM, it was possible to classify the dimensionality over periods at each station along all profiles, as shown in Figure 6.1. The phase tensor representation for dimensionality is shown in Figure 6.2 (generated with the MTPy package (KRIEGER and PEACOCK, 2014)).

From the results obtained by WALDIM, we can see a predominance of 1D dimensionality for shorter periods in the three profiles and a predominance of 3D dimensionality for longer periods. Similarly, the phase tensor presents non-zero values for the skew angle β and flat ellipses for long periods in all three profiles. Thus, we classify the data with strong three-dimensional influence, justifying the application of a 3D inversion methodology.

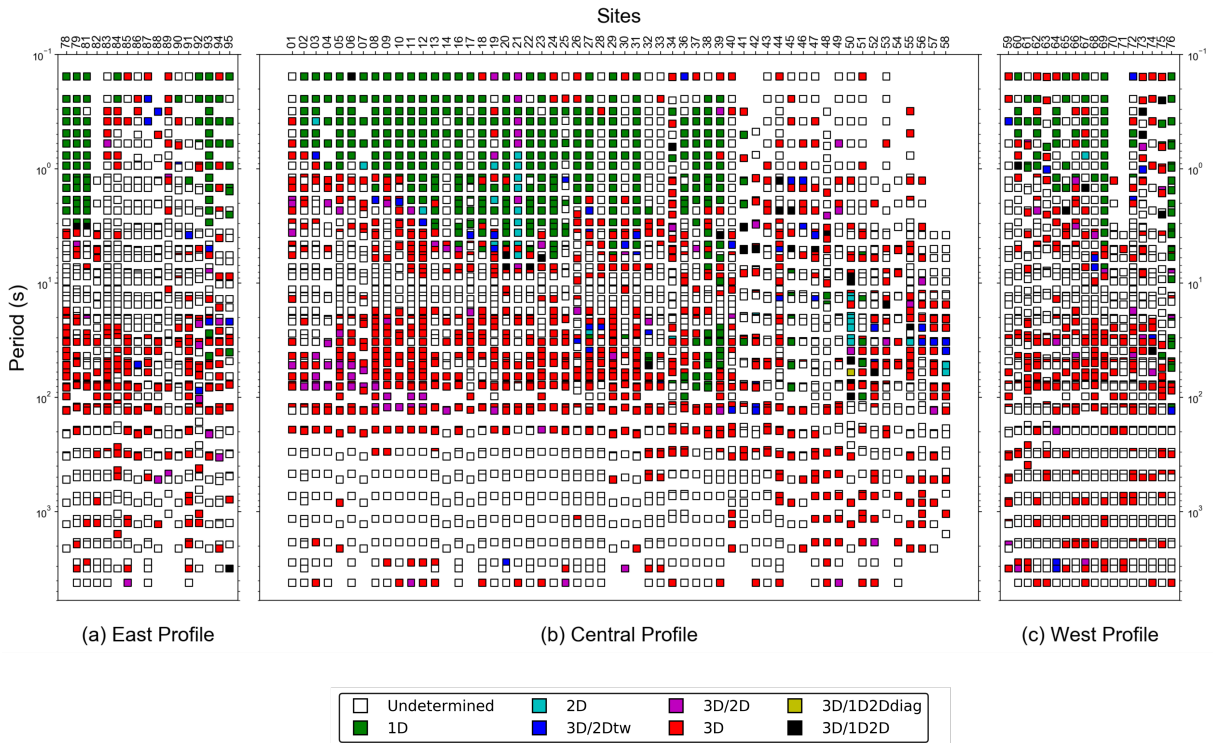


Figure 6.1: Dimensionality analysis of geoelectric structures by period of each station for the three profiles using the WALDIM code (Martí et al., 2009).

6.2 Data Preparation

To prepare the data for inversion, we used the 3D-Grid software (Naser Meqbel, personal communication). The 3D-Grid not only works to facilitate the setting of data file format, but also helps to construct model and covariance files that will be used as input for ModEM (and we also used it in the two next sections). It has

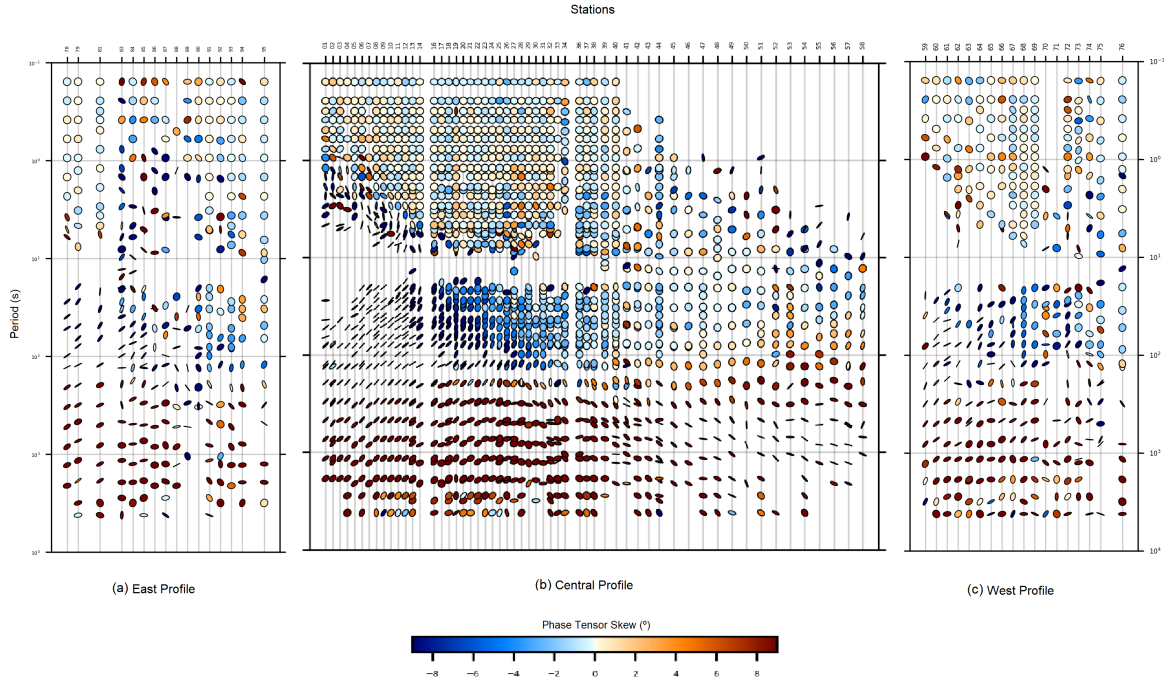


Figure 6.2: Dimensionality analysis of geoelectric structures by period of each station for the three profiles employing the skew angle β of the phase tensor. This image was generated using the MTPy package (Krieger & Peacock, 2014).

an interactive graphical interface, allowing the 3D visualization and edition of these files. The software is based on Windows Operating System and has a free academic version.

In general, the data have good quality. The stations located in the shallow part of the profile had noisy data points around the period of 10 s, which were removed. These noises were associated with the influence of microseisms in the ocean floor. Besides this visual inspection, we point out four main concerns regarding the data selection that might be considered for inversion.

Sites with very noisy data points may be excluded to proceed to inversion. In this subjective decision, it must be taken into account the quantity of available sites and how much of real information each site is providing. In our case, all 90 sites were considered good and were included in the inversion.

Another concern is the choice of periods that is relevant to the inversion process. In ModEM (and in most of 3D MT inversion codes), the computational cost, in terms of required number of nodes (processors), is dependent of the number of periods. A data set may have two or more very close values of period providing overlapping information, but yet they are considered as separate periods. Reading our data, 205 different periods were mapped between approximately 10^{-1} to 10^4 s over the 90 sites. As this large number of periods is unnecessary and exceeds the computational capacity of the PC cluster, we decided to interpolate the data. Using 3D-Grid, we

applied a linear spline interpolation using 6 periods by decade, resulting in a total of 26 periods. The required number of processors is calculated by two times the number of periods plus one, meaning that the inversions were run on 53 processors.

Next, the data components to be included in the inversion also must be considered. In our case, the vertical component of the magnetic field was not acquired, thus the vertical function was not included in the inversion. However, instead of using only the off-diagonal components of the impedance tensor for inversion (as in LINDSEY and NEWMAN (2015)), we decided to invert the full impedance tensor. Despite the small values of the diagonal elements and the fact that they are relatively noisy, their non-zero character is what differ a 3D from a 2D situation. Indeed, it is possible that considering only the off-diagonal elements for inversion leads to loss of subsurface information as showed by PATRO and EGBERT (2011).

And last, but not least, it is important to set up the data error to be considered in the inversion. Here, we set the maximum value between the original data error and error floors. We assign error floor values of 10% of $|Z_{xy}Z_{yx}|^{1/2}$ for the diagonal elements of the impedance tensor, 5% of $|Z_{xy}|$ for Z_{xy} and 5% of $|Z_{yx}|$ for Z_{yx} .

6.3 Mesh Design

As the three-dimensional inversion itself is computationally very expensive, taking into account the complexity of the algorithm (as discussed in Section 5.3), it is also important to be careful in the definition of the mesh design to be used in the starting model. While finer models can be more accurate and demand unrealistic computing memory and time, coarse mesh requires less computational power but it can lead to low resolution and high misfit values. Likewise, large models requires high computational cost. The grid size increases with the addition of padding cells around the area of interest, used as a way to avoid boundary effects. The grid discretization has to be chosen based on the site spacing and model resolution. The inclusion of topography and/or bathymetry also overcharges the model.

Considering all mentioned above, we tested some grid discretization and chose a mesh consisting of 61 cells in the x-direction and 44 cells in the y-direction in the area of interest, each cell has a horizontal size of 1969 m x 1969 m that increases towards the edges of the model by a factor of 1.3 in a range of 17 cells for both directions; and, in the z direction, we established a total of 100 layers starting by a layer with 1 m thickness increasing smoothly by a factor of 1.12, resulting in a model with 95 x 78 x 100 cells (in x , y and z directions respectively) and covering an total area of 1579 x 1546 km² extending to 696 km of depth. Also, we included the local bathymetry with 0.3 Ω .m of resistivity for the seawater, ensuring to project the sites on top of the Earth. Since ModEM only allows sites positioned in different

cells in the grid, this condition also was verified in 3D-Grid.

6.4 Initial models

As well highlighted by DONG and JONES (2018), an inappropriate initial model may cause the inversion to generate artifacts. The iterative optimization method used in ModEM is dependent of an starting model. In regions of the model where few information is available to restrict the results, the inversion algorithm tends to recovery the initial resistivity values provided in the starting model.

Hence, a common and recommended practice is to start by the simplest model, such as a homogenous half-space (mainly when limited or no prior information is available), and to assign the model background resistivity based on the average resistivity of the observed data. Also, it is usual to compare results using different initial models. Starting the inversion with complex models can produce unreliable structures into the results.

We chose to start with a homogeneous half-space, but testing for different background resistivity values. Based on the average resistivity of the data, we used two different initial models: 10 and 50 Ω .m homogeneous half-space. For both, the local bathymetry was fixed with a value of 0.3 Ω .m for the electrical resistivity of the seawater.

6.5 Inversion Parameters

As 3D inversion has many more parameters that can freely vary involved in the calculations than in a 1D or 2D inversion, the first requires robust stabilizing functions (MIENSOPUST (2017)). In order to attend this requirement, ModEM is implemented with regularization and smoothness criteria as explained in Section 5.3. Here, we tested three different initial regularization parameter (λ) values for each initial model: 1, 10 and 100. The software standard smoothing parameter of 0.2 for all directions were considered for all tests.

Regarding the stopping criteria, the threshold value for nRMS was 1.05, for λ was 1×10^{-8} and the maximum number of iterations was set as 400.

6.6 Results of the 3D Inversion

A total of six inversion results are shown in this section. Table 6.1 summarizes the chosen inversion parameters and the obtained number of iterations, starting and final nRMS values for each test. Among the three stopping criteria mentioned

above, all tests reached the value of 1×10^{-8} for λ . All of them resulted in similar final nRMS values and similar features in the geoelectrical models as can be seen in Figures 6.3 and 6.4. Therefore, we established some criteria to choose our preferred final model.

Initial Model \ Initial λ	1	10	100
10 Ω .m (nRMS ₀ = 17.4421)	56 iterations nRMS = 1.7483	80 iterations nRMS = 1.6221	102 iterations nRMS = 1.5384
50 Ω .m (nRMS ₀ = 36.8107)	75 iterations nRMS = 1.5829	82 iterations nRMS = 1.6288	123 iterations nRMS = 1.6997

Table 6.1: Summary of the number of iterations and final nRMS value obtained after run the inversion with the different combinations of initial models and λ values. The subindex 0 indicates the initial value of nRMS.

The starting nRMS for the 10 Ω .m and 50 Ω .m homogeneous half-space are 17.4421 and 36.8107 respectively. Thus, we choose the initial model with the minimum starting nRMS value (10 Ω .m half-space). Among the three results with this model (Figure 6.3), changing only the initial regularization parameter λ , very few differences were noted. For higher values of initial λ , the features become slightly smoother. Also, for larger values of λ , the required number of iterations increases. Therefore, we decided to choose the medium value of initial λ (10) that results neither so smooth nor so rough features and a reasonable number of iterations.

In Figure 6.5, we can observe all inversions converged quickly to relatively small nRMS values. Considering the good quality of the data, we expected nRMS values less than two being satisfactory. The distribution of nRMS value for each site are basically the same for all tests (Figure 6.6). Obtaining similar values of nRMS means similar fit between the observed and predicted apparent resistivity and phase curves as can be seen in some examples in Figures 6.7 and 6.8.

Another criterion used to check out our best final model was the comparison between the resistivity values from an available well log data and from our final models. The induction log of the well sps42, with a depth range of 1.39 to 5.39 km, is located at the same point of site 45 from the central profile. With this, we extracted the values of resistivity in depth at the site 45 location of each 3D resulted model and plotted to compare with the induction log data. Of course, the values are not expected to be the same, once, in a well log data, the measured resistivity values are pontual and does not take into account the regional resistivity. However, we expected that the curves of resistivity from the inversion results follow the overall trend of the well log data. Thus, in Figure 6.9, we can see that the curve obtained from the inversion with 10 Ω .m half-space and 10 value of initial λ (black line) is

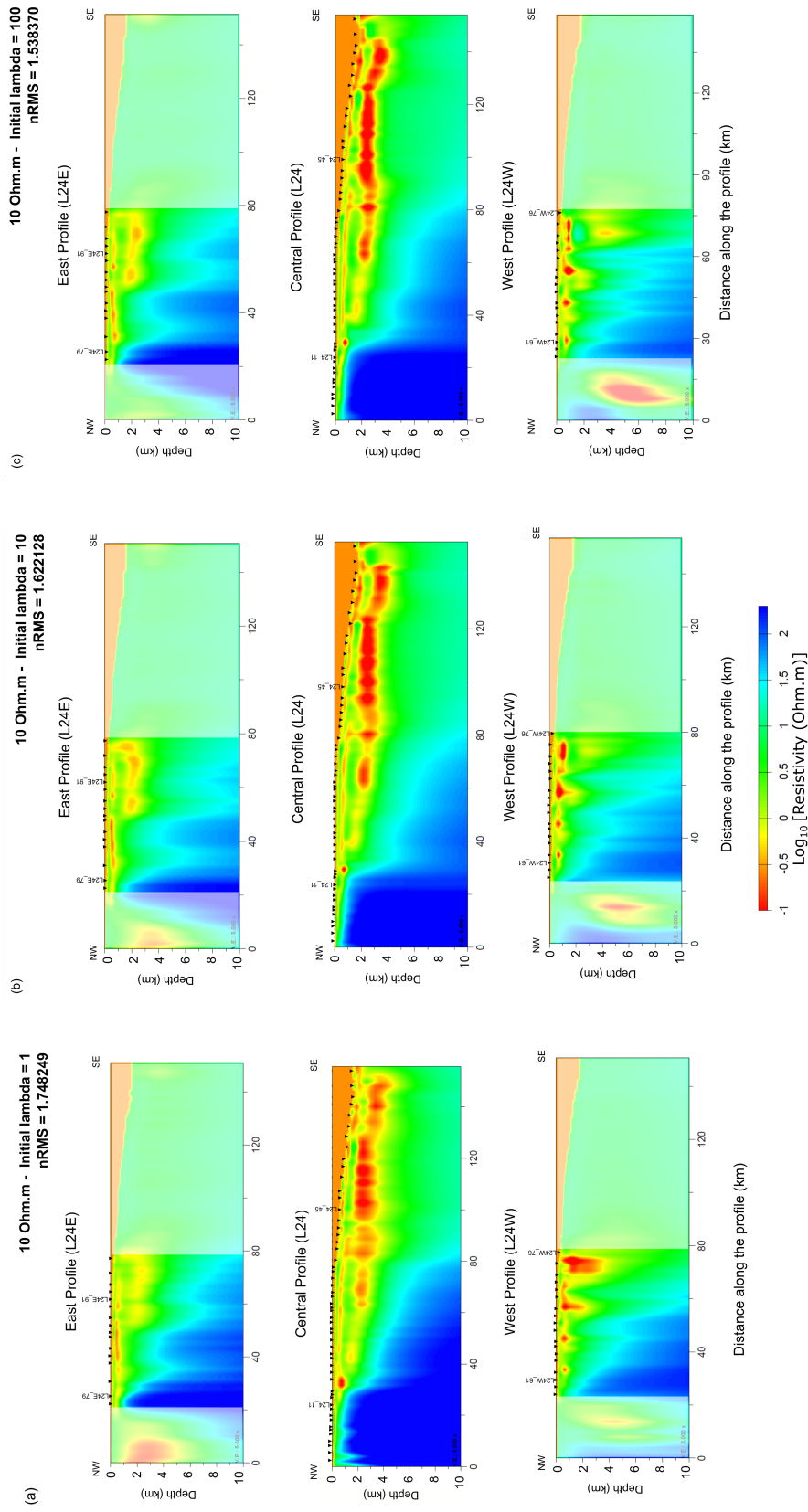


Figure 6.3: Sections from the 3D final models for all profiles using the initial model of 10 Ω .m for initial λ values of: (a) 1; (b) 10; and (c) 100. The lateral profiles have stations only in the distance from 20 to 80 km approximately. The white rectangles in it indicate the part of the profiles must be neglected.

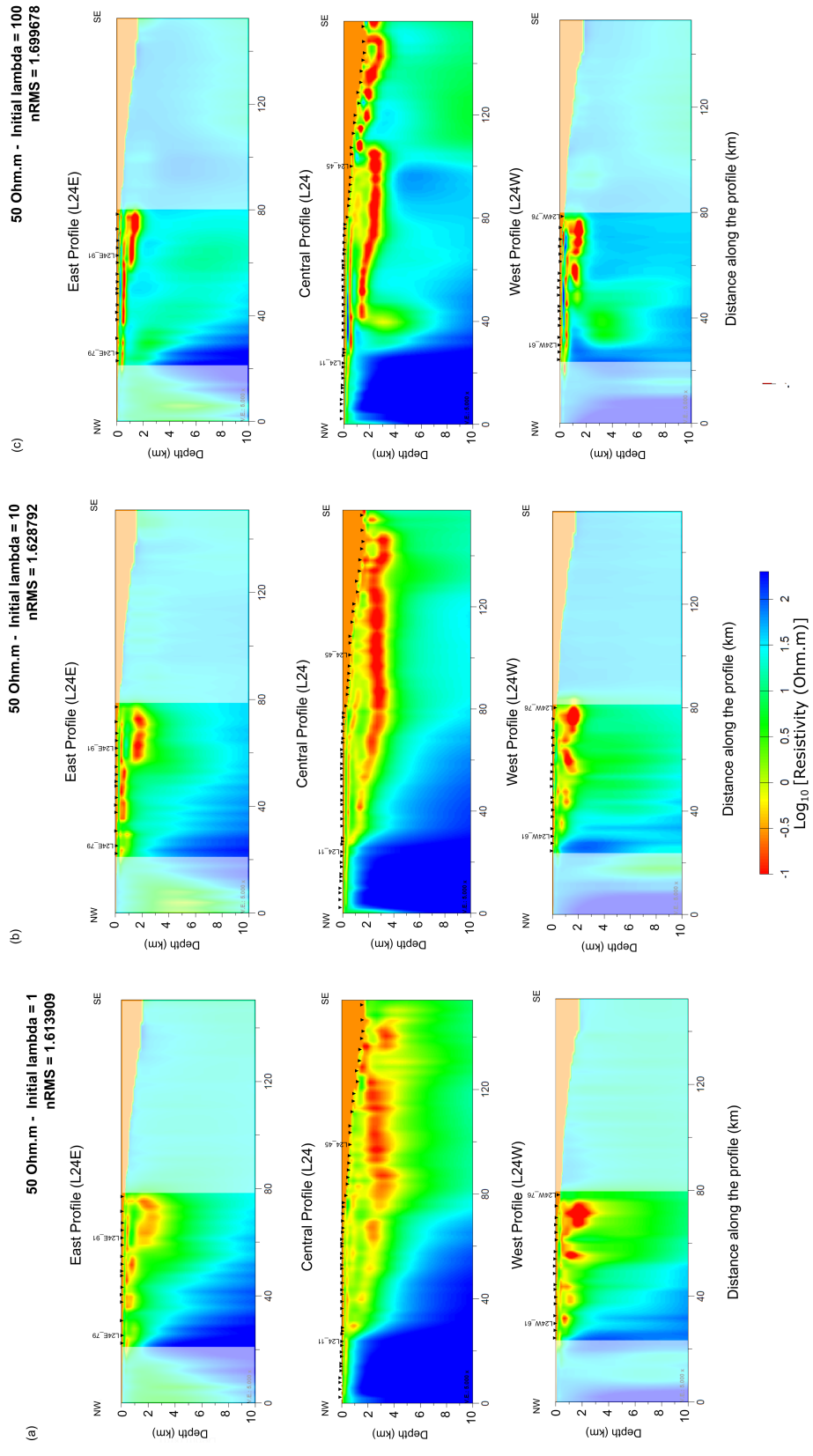


Figure 6.4: Sections from the 3D final models for all profiles using the initial model of 50 Ω .m for initial λ values of: (a) 1; (b) 10; and (c) 100. The lateral profiles have stations only in the distance from 20 to 80 km approximately. The white rectangles in it indicate the part of the profiles must be neglected.

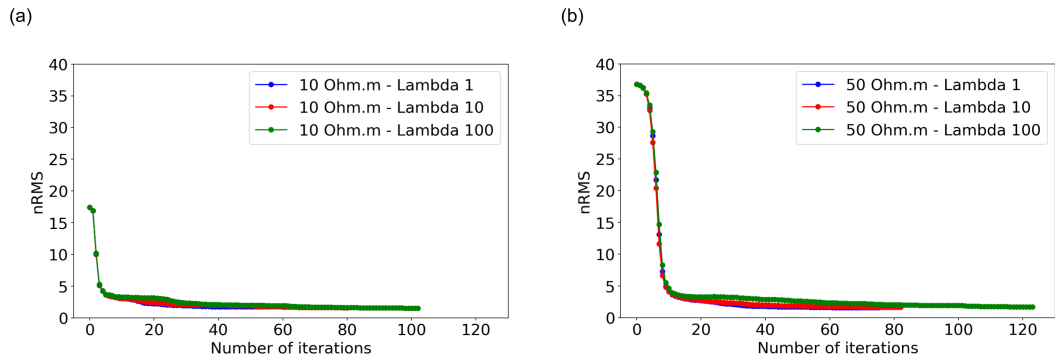


Figure 6.5: Graphic of nRMS values versus number of iterations for: (a) the initial model of 10 Ω .m and different initial λ values; and (b) the initial model of 50 Ω .m and different initial λ values.

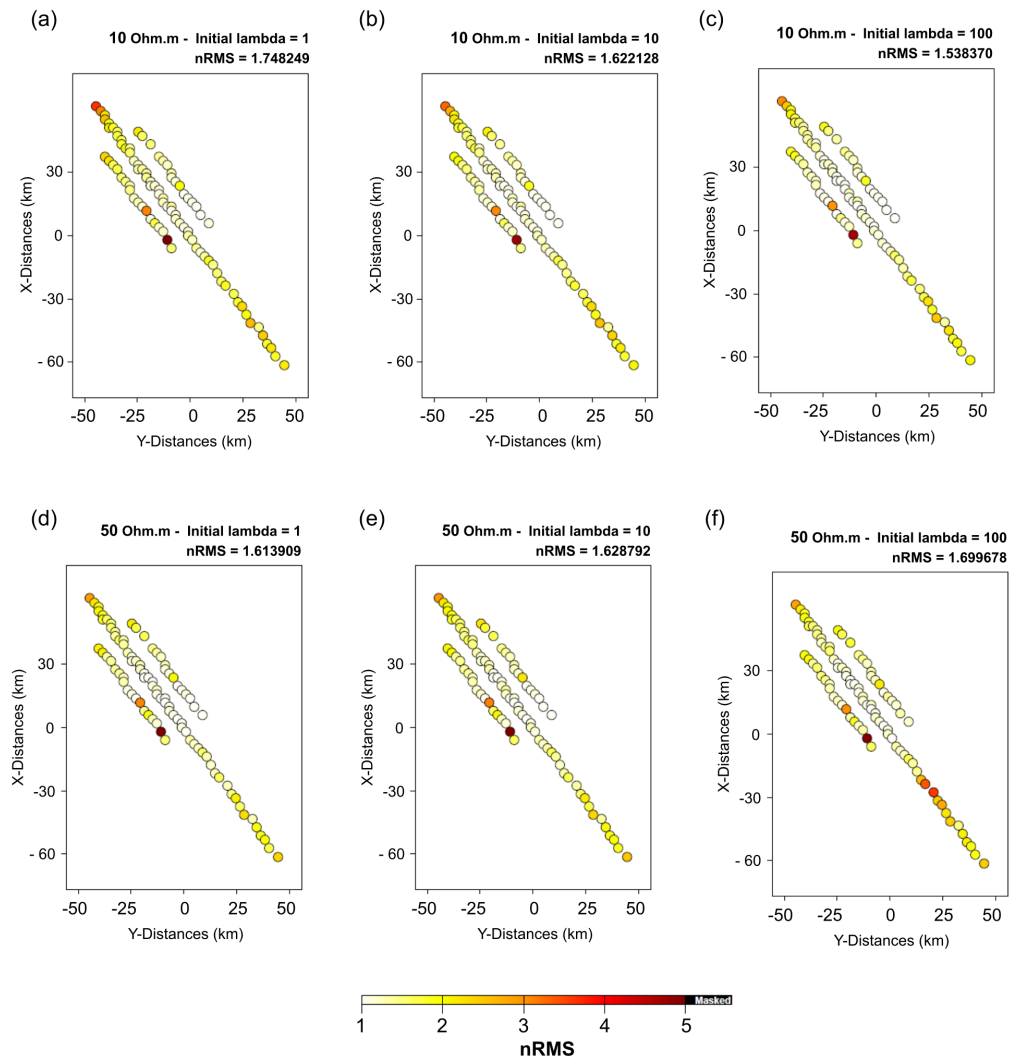


Figure 6.6: Normalized root mean square (nRMS) misfit for the full impedance tensor at each site in all three profiles obtained by inversion with the six different inversion tests carried out.

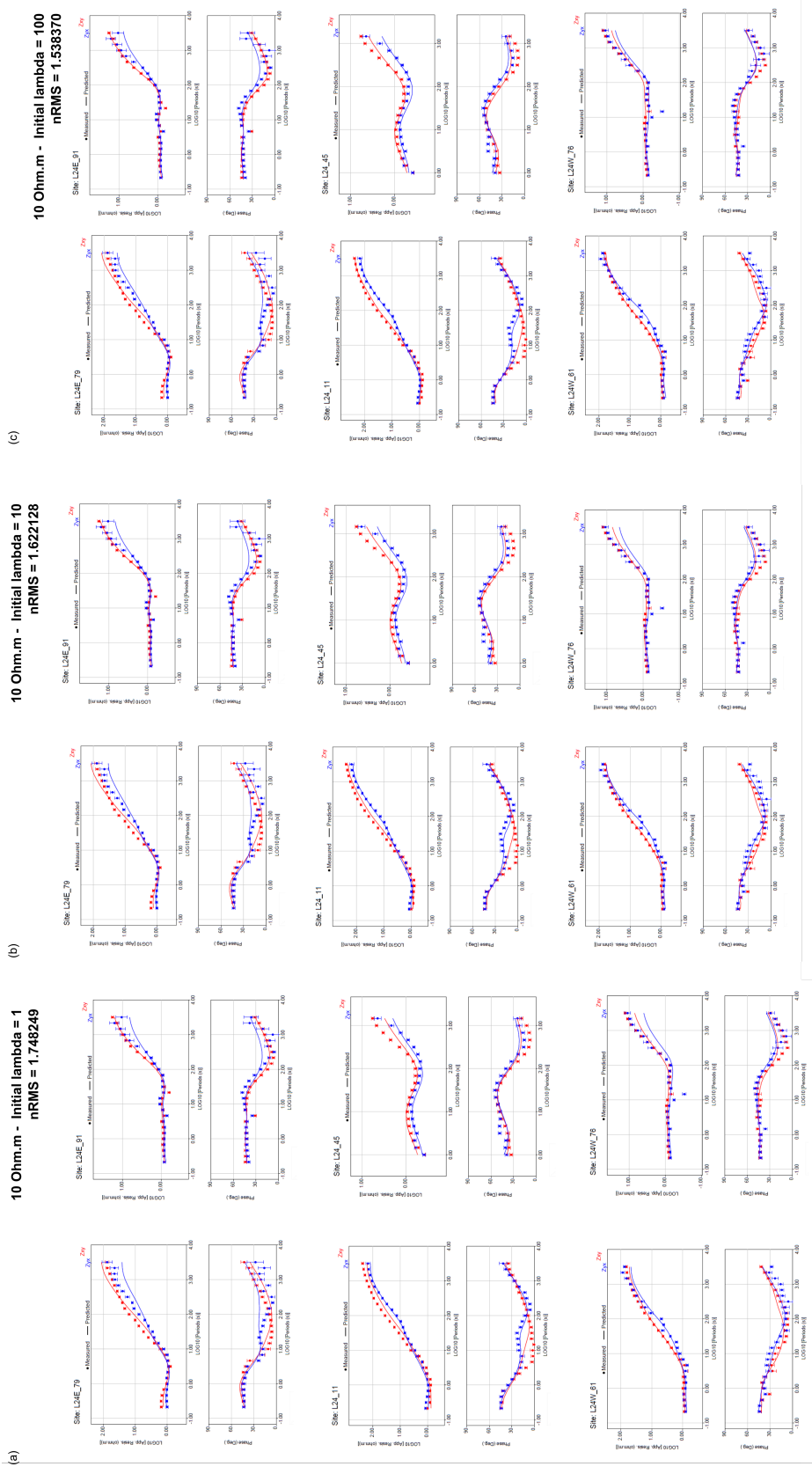


Figure 6.7: Apparent resistivity and phase curves for the stations L24E_79, L24E_91, L24_45, L24W_76 and L24W_81. The dots represents the observed data and the line represents the predicted data obtained by inversion with the initial model of 10 Ω .m and initial λ values of: (a) 1; (b) 10; and (c) 100.

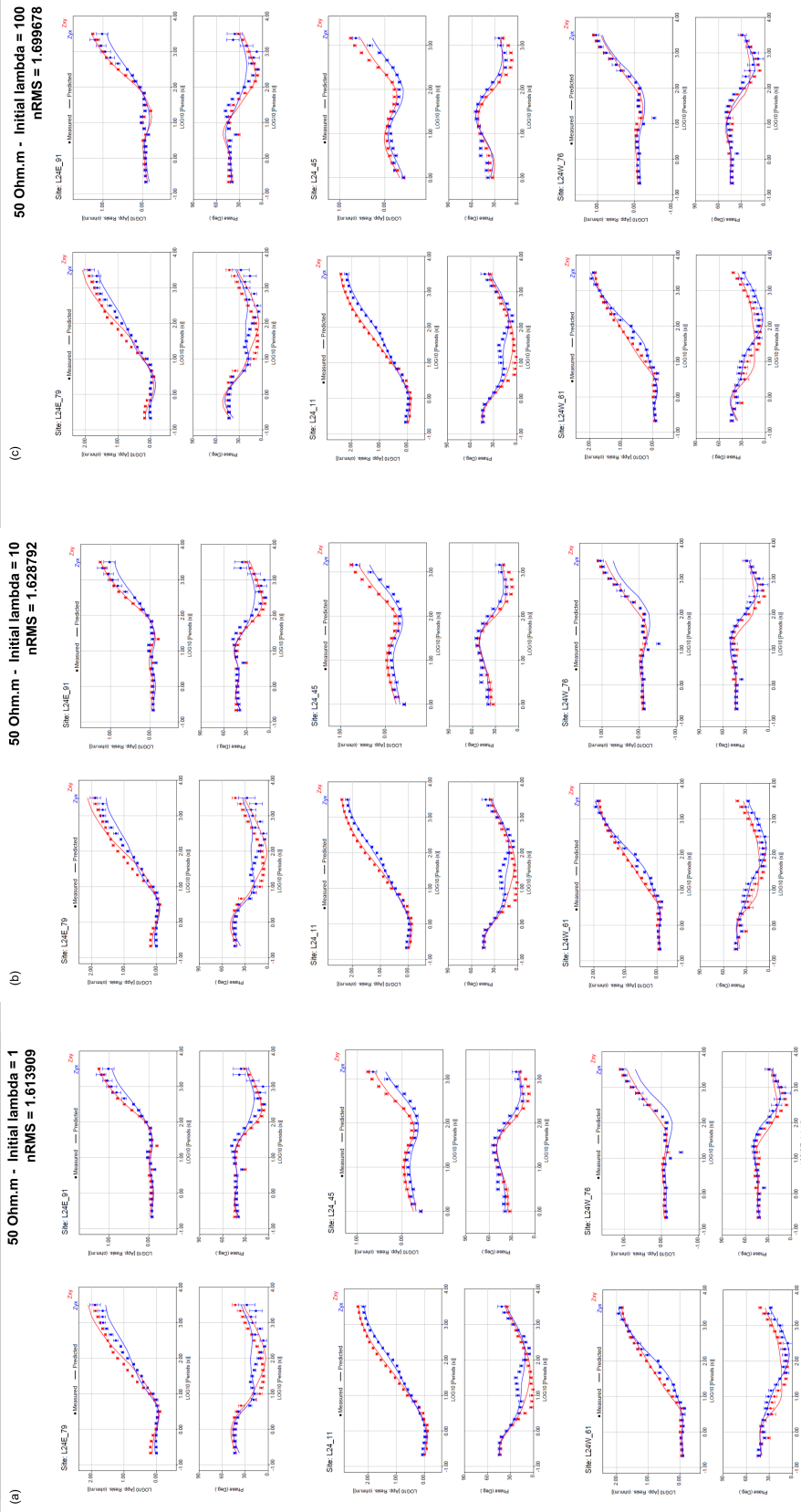


Figure 6.8: Apparent resistivity and phase curves for the stations L24E_79, L24E_91, L24_11, L24_45, L24W_61 and L24W_76. The dots represents the observed data and the line represents the predicted data obtained by inversion with the initial model of 50 Ω .m and initial λ values of: (a) 1; (b) 10; and (c) 100.

the best fitted³.

Figure 6.10 (a) displays the vertical slices of our preferred model along all three profiles (as in Figure 6.3b), where we have identified three main geoelectrical units delimited by the gray dashed lines.

6.6.1 Low resistive unit

The low resistive unit is characterized by the predominance of electrical resistivity values less than $1.0 \Omega.m$.

In the central profile, this sequence presents depths ranging from around 500 m in the northwestern portion up to 4 km in the southeastern part. Two main conductors C1 and C2 are highlighted. C1 is a very thin flat layer situated directly below the seafloor. It has resistivity of $1.0 \Omega.m$ becoming more conductive seawards (up to $0.1 \Omega.m$). C2 is a thicker layer with about 1.5 km of thickness and has a lateral continuity from 60 to 140 km along the central profile. This is the highest conductive feature of the entire model with less than $0.2 \Omega.m$.

In the east profile, two features is likely to be a lateral continuity of C1 and C2 due to the position and resistivity values. The same is noted in the west profile only for the C1 conductor. C1 seems thicker in the west profile compared to the others.

6.6.2 Intermediate resistive unit

Between the dashed lines, it is located the unit of resistivity values between 1 and $10 \Omega.m$. In the southeast portion of the central profile, a vertical body with the same intermediate resistive character, labelled by a question mark, seems to be an uplift of the horizontal layer.

6.6.3 High resistive unit

We classified features with resistivity greater than $10 \Omega.m$ as a high resistive unit (below the second gray dashed line) and in it there are three subdivisions R1, R2 and R3.

The resistor R1 exceeds $200 \Omega.m$ (highest resistivity). In the central profile, R1 has a rectangular shape and is located at the northwest portion of the line between 0 and 20 km. It starts at less than 1 km of depth and extends downwards. A lateral continuity of it is noted in the east profile, but not in the west profile.

R2 ranges from about 50 to $200 \Omega.m$. Its top starts at 3 km of depth and down dips towards southeast direction to 6 km of depth in the central profile where

³All observed and predicted apparent resistivity and phase curves obtained from the inversion of the $10 \Omega.m$ homogeneous half-space with initial λ value of 10 are presented in the appendix of this work.

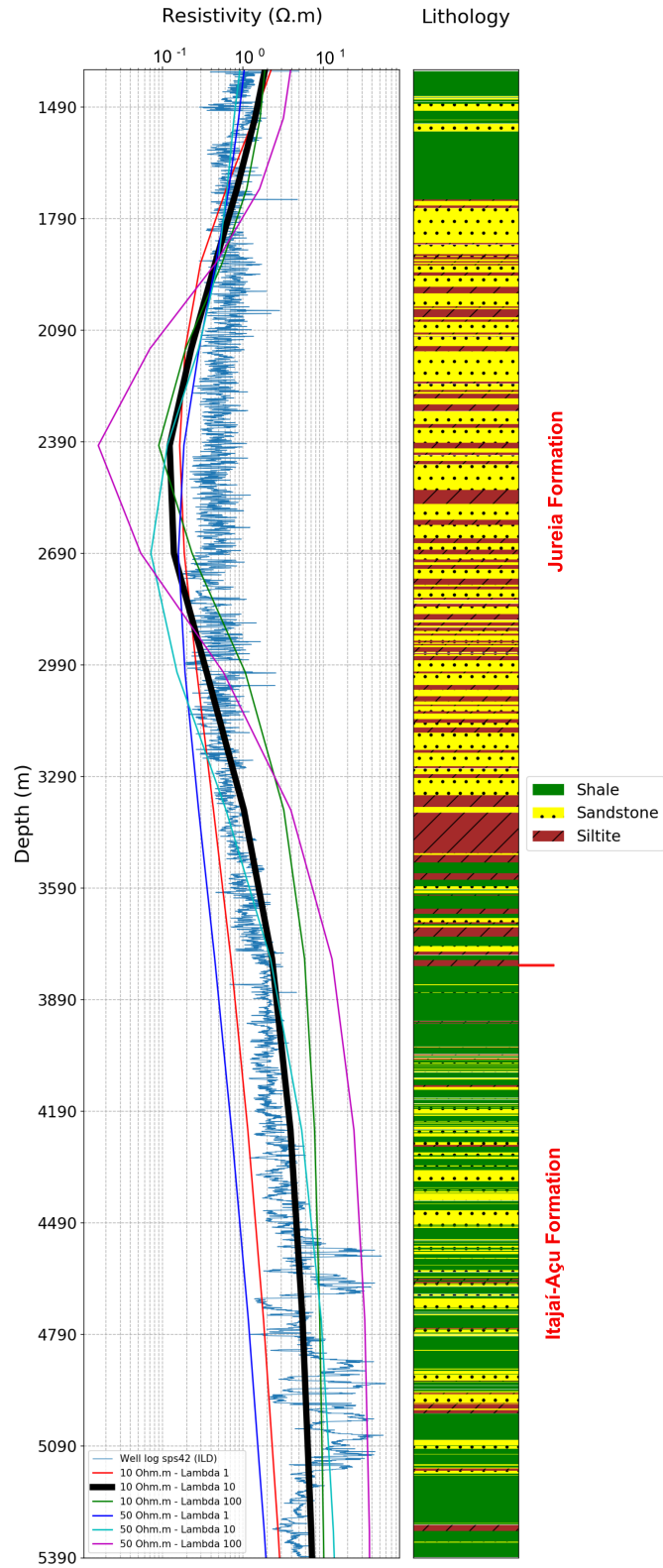


Figure 6.9: Comparison between resistivity log from well sps42 and resistivity values derived from the MMT inversion tests along site L24_45 at the same location. The thick black line represents the preferred model result at the well log location. Right image is a lithology column from the sps42 borehole. The resistivity and lithology information of the well sps42 were obtained from the Petroleum National Agency (ANP).

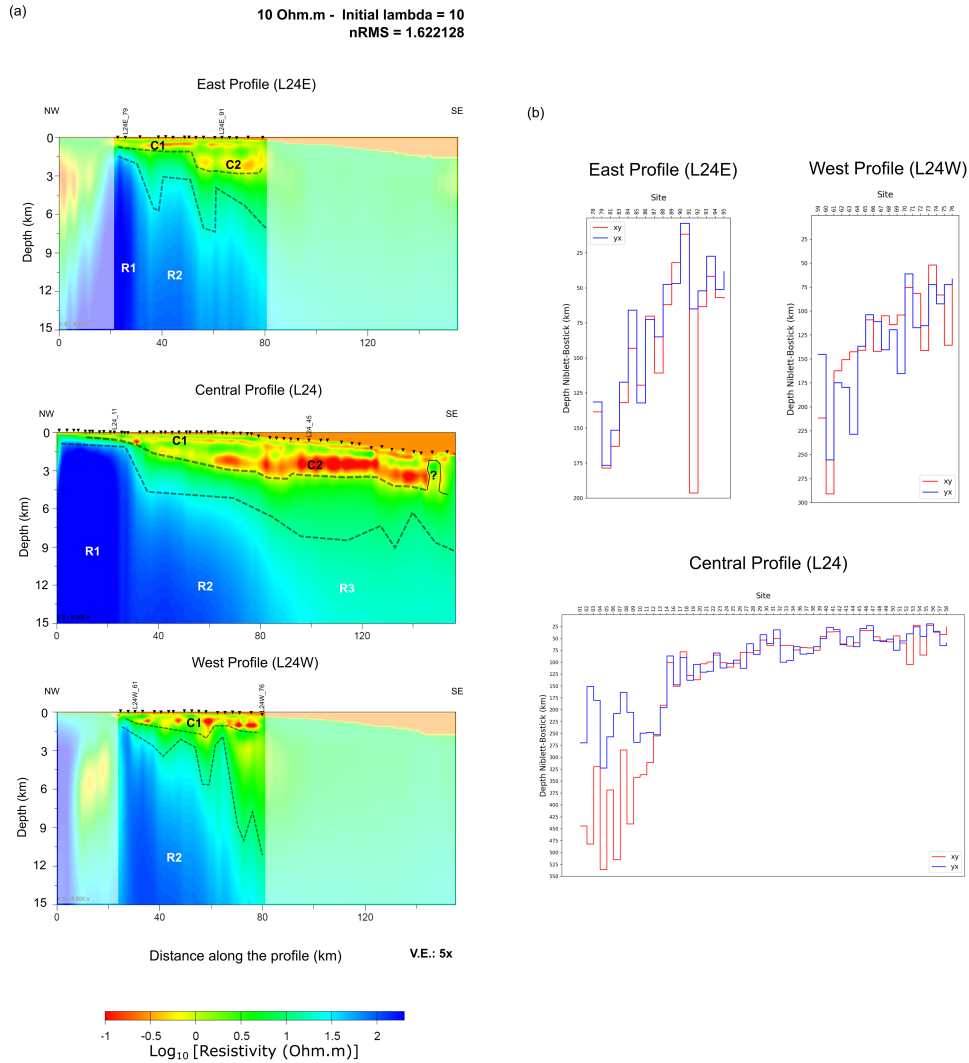


Figure 6.10: (a) Vertical sections from the 3D final model along the three profiles using the initial model of 10 Ω .m for initial λ value of 10, chosen as our preferred model (as in Figure 6.3b), with labels of the main geoelectrical units. The gray dashed lines separate a low, an intermediate and a high resistive zone. C1 and C2 identify the pronounced conductors; R1, R2 and R3 the resistors; and the question mark the relatively resistive vertical feature delineated by a filled black line. The lateral profiles have stations only in the distance from 20 to 80 km approximately. The white rectangles in it indicate the part of the profiles must be neglected. (b) Maximum depth of penetration for xy and yx directions of each site estimated from the Niblett-Bostick depth approximation.

it extends from 20 to 80 km of profile distance. It has a significant gradational variation in the resistivity values noted also in the lateral profiles.

R3 is limited by resistivities between 10 and 50 Ω .m. It is a weak resistor starting from 6 km of depth and positioned from 80 km of the central profile. The lateral profiles does not have MMT sites from this distance, consequently, they do not show evidence of R3 feature.

The lateral continuity of the features cited above can also be noted at the horizontal slices of our preferred model (Figure 6.11). In the first three slices, the continuity of the shallow conductors is very clear. The resistor appears at depths greater than 1 km and it is extended to the continent. The two conductors that are evident in the last three slices are inversion artifacts.

Figure 6.10 (b) shows the maximum depth of penetration for xy and yx directions of each site based on the Niblett-Bostick depth approximation (NIBLETT and SAYN-WITTGENSTEIN (1960); BOSTICK (1977)). The maximum penetration depths presents a large variation due to its dependence on the apparent resistivity related to the longest period of each site. As the resistivity decreases towards the southeast direction, the maximum penetration depth also decreases. However, most of the sites have penetration depths greater than 25 km validating the data sensibility from our models that reach 15 km of depth.

6.7 Comparison with previous results

GALLARDO *et al.* (2012) presents results of a separate 2D magnetotelluric inversion (based on SMITH and BOOKER (1991) approach) and a joint inversion of seismic reflection, magnetotelluric, gravity and magnetic data from the main profile that are displayed in Figures 6.12 and 6.13 respectively.

A comparison of Figure 6.12 and Figure 6.14 shows that the 2D model is smoother than the 3D model. The detailed seen in our preferred model at shallow depths differentiating the C1 and C2 units are not observed in the 2D model. Both results show the gradational variation of the resistivity values towards southeast of the large resistor in the left corner.

Comparing now Figures 6.13 and 6.14, we can see analogous features. A and B in the joint model seems to be the same conductors C1 and C2 that we found in our preferred model. F and E are similar to our R1 feature. However, the uplift noted by the question mark in the end of our model is not expressed in the joint model. As units C and D are distinct by density properties (Figure 6.13b), our 3D model was not capable to classify these two features.

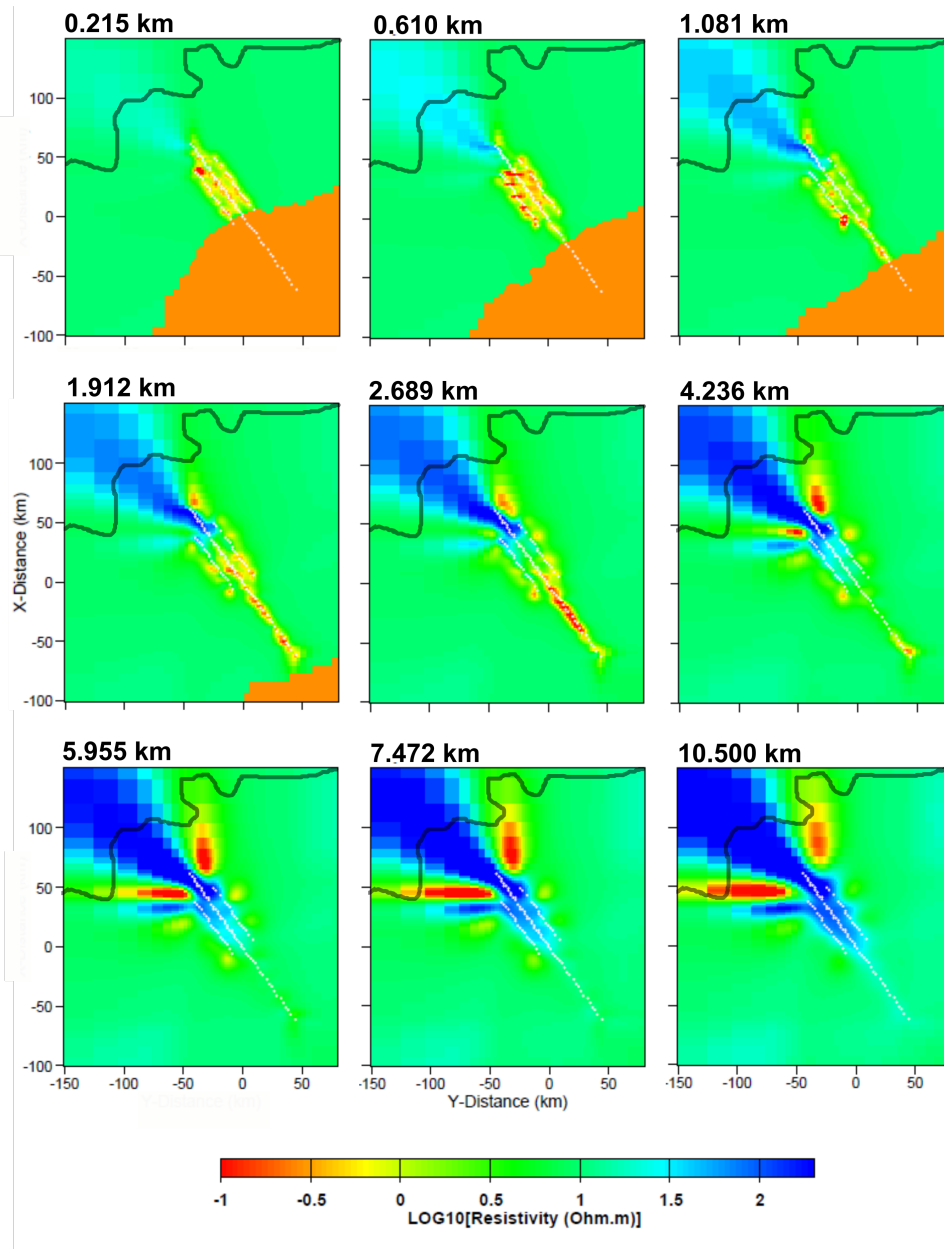


Figure 6.11: Depth slices from our preferred final model. The black line delineates the coast line and the orange color represents the seawater.

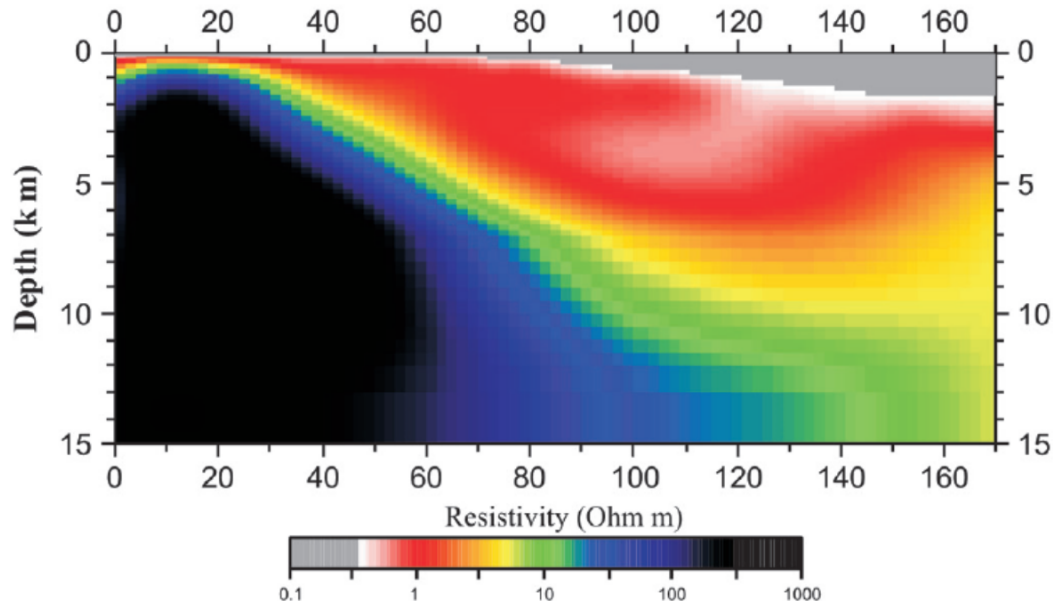


Figure 6.12: NW-SE section of the electrical resistivity model obtained from a separate 2D magnetotelluric inversion based on SMITH and BOOKER (1991) approach. (Source: GALLARDO *et al.* (2012))

6.8 Interpretation

The right side of Figure 6.9 exhibits the lithology information of the well log sps42. In addition, a previous interpretation based on the seismic line coincident with the MMT central profile location is shown in Figure 6.15 (DE LUGAO *et al.*, 2008). The location of the MMT sites and the well log sps42 are marked at the seafloor in this geologic section. With it, we draw some correlations between our 3D inversion result and the geologic setting.

Clearly, the resistive unity represents the crystalline basement. In the literature, as described in Chapter 3, the Pre-cambrian granites and gnaisses of the Ribeira Belt form the basement. The Ribeira Belt is also noted by PANETTO *et al.* (2018) that describes 3D magnetotelluric images situated at the southeast Brazilian coast that can be interpreted as an onshore extension of our studies. The lateral variation of resistivity noted in this unit can be caused by the geometry of the basement. MODICA and BRUSH (2004) describes regional uplift events that probably affect the structure of the Ribeira Belt forming faults, horsts and grabens filled by posterior sedimentary deposition.

The conductors C1 and C2 do not exhibit the same clear correspondence with the geologic section. However, the well log crosses C2, situated between approximately 1.5 km to 3.5 km depth. This unit presents very high conductivity values and coincides the sandstones intercalated by thin siltite layers of the lithology column within the Jureia Formation (MOREIRA *et al.*, 2007). This high conductivity may

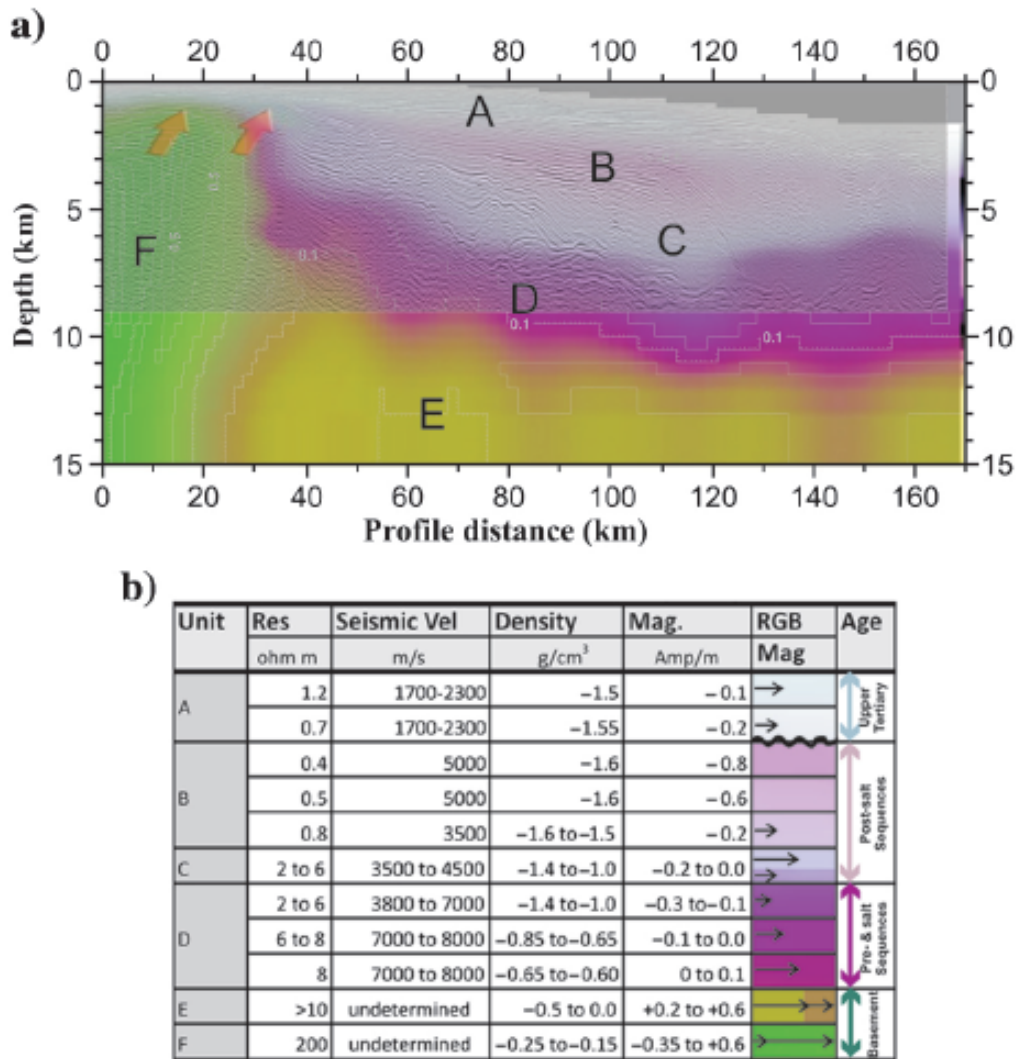


Figure 6.13: (a) Geospectral image of joint inversion overlain by a migrated seismic section (FONTES *et al.*, 2009). Resistivity, seismic slowness and density are illustrated in RGB and magnetization in contours spaced every 0.2 Amp/m. (b) Table illustrating the annotated zones and corresponding property ranges in the image above. The colors in the geospectral column match those represented in (a) whereas the magnitude of vectors represent the magnetization contrast. (Source: GALLARDO *et al.* (2012))

be indicative of seawater content. Whereas, the low resistivity of C1 and its shallow position is indicative of the recent sediments of the Itamambuca Group (MOREIRA *et al.*, 2007) referred in the geologic section as a Cenozoic sequence. This group is characterized by proximal alluvial fans and sandstones and pelites deposited in bathyal zones with mixed carbonatic sedimentation near to the platform (GARCIA, 2012).

In the lithology column, at depths deeper than 3.3 km, the sandstones filled by seawater is becoming less dominant in the lithology column, showing an increase of the resistivity values. At this level, the presence of shale layers are more evident with some dispersed sandstones (typical of the Itajaí-Açu Formation). This region is

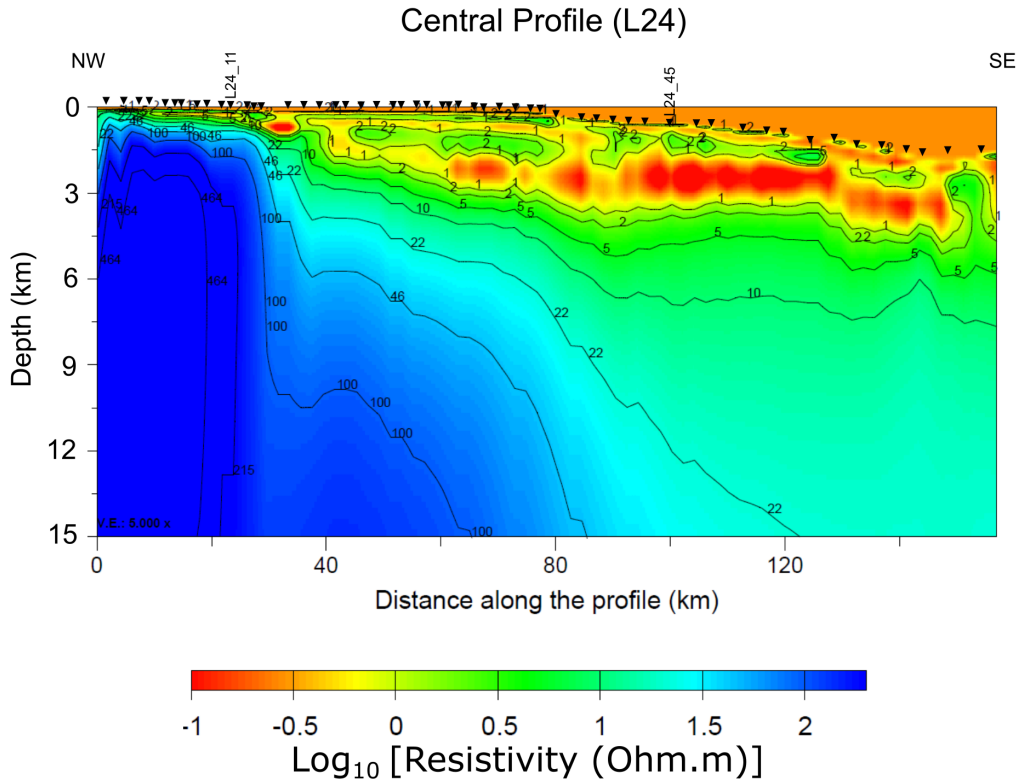


Figure 6.14: Section from the 3D preferred final models for the central profile with contour lines added.

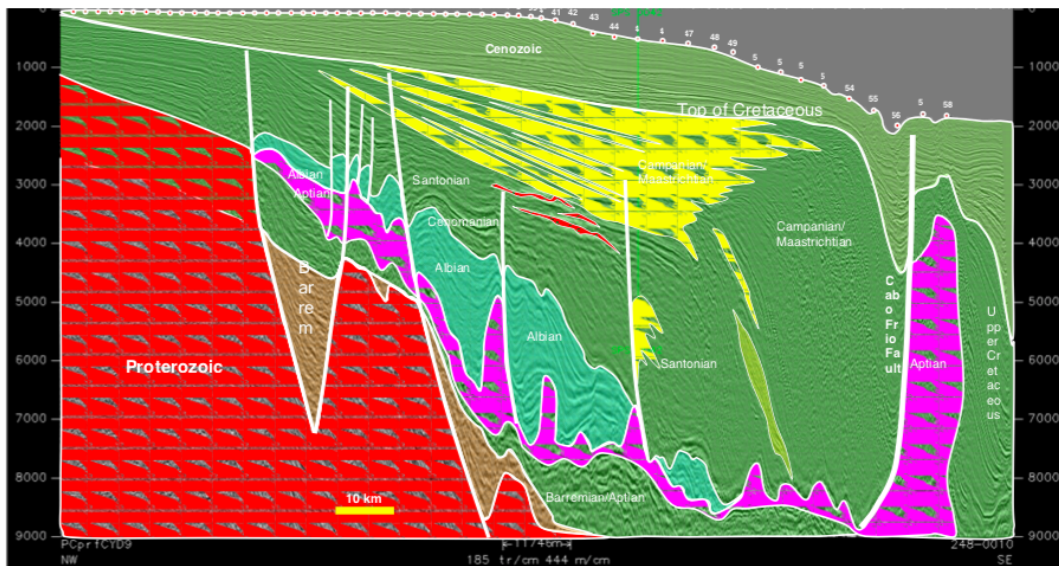


Figure 6.15: Geological interpretation based on a seismic line located at the same position of the MMT central profile. The MMT sites are drawn in the ocean seafloor. (Source: DE LUGAO *et al.* (2008))

located below the C2 layer, with resistivity from 1 to 5 Ω .m in our preferred model.

The question mark can be associated with the Cabo Frio Fault and the salt diapir shown between sites 56 and 57 in the seismic-based geologic section. This

vertical structure is also very evident in Figure 6.14, where this feature is delimited by the contour lines. The development of the Cabo Frio Fault is associated to the salt tectonics and delineate the transition between the extension and contraction detached on salt (MOHRIAK *et al.* (1995); GUERRA and UNDERHILL (2012)).

Chapter 7

Conclusions

The MMT measurements performed along three profiles at the Santos Basin presented 3D electrical structures associated with the complex geologic setting of the region that were mapped by using a tridimensional inversion scheme. To apply the 3D inversion a careful data preparation, grid discretization, and definition of initial models and inversions parameters were needed. Comparison between the different results, obtained by using different initial models and starting regularization parameters, allowed the analyses of the inversion algorithm behavior.

The preferred final model showed geoelectrical features in good agreement with the seismic interpretation for the same profile. The resistive basement is evident in the northwest portion of the main profile, the conductive layers is associated to the seawater-filled sandstones and shales and the vertical intermediate resistive body in the southeast portion of the profile is most likely related to the salt structure. The identification of these features, concerning the geology, agree with studies proposed by other authors (MOHRIAK *et al.* (1995); MODICA and BRUSH (2004); MOREIRA *et al.* (2007); GARCIA (2012); GUERRA and UNDERHILL (2012); PANETTO *et al.* (2018)).

Based on these results, we conclude that the MMT application to exploration environments contributes to clarify the geologic structures in subsurface. An improvement in image resolution from our 3D model compared to 2D previous results is also notable and represents a contribution from our studies. The evident salt diapir in our 3D result is not mapped by GALLARDO *et al.* (2012).

However, the method also presents its limitations mainly in deeper ocean where its sensitivity is reduced by the attenuation of the natural electromagnetic signal. The differentiation between the salt and pre-salt layers could not be resolved. To overcome this limitation, we suggest the employment of controlled-source electromagnetic (CSEM) method in association with the MT method aiming at improving the imaging of features beneath the salt layer. Additionally, a denser array of MMT sites might also enhance the characterization of the pre-salt structures.

Finally, our study shows the importance of understanding the influence of each procedure in the 3D MT inversion. Future studies should test more parameters such as the use of more complex initial models and different smoothing parameters and see how it affects the final result. Furthermore, this dissertation collaborates to the discussion of the strengths and weaknesses of the 3D MT inversion which is currently experiencing a fast growth thanks to continuous advance in optimization algorithms and computer power.

Bibliography

- ASMUS, H. E., BAISCH, P. R., 1983, “Geological evolution of the Brazilian continental margin”, *Episodes: Journal of International Geoscience*, v. 1983, n. 4, pp. 3–9.
- AVDEEV, D., AVDEEVA, A., 2009, “3D magnetotelluric inversion using a limited-memory quasi-Newton optimization”, *Geophysics*, v. 74, n. 3, pp. F45–F57.
- AVDEEV, D. B., 2005, “Three-dimensional electromagnetic modelling and inversion from theory to application”, *Surveys in Geophysics*, v. 26, n. 6, pp. 767–799.
- AVDEEV, D. B., KUVSHINOV, A. V., PANKRATOV, O. V., et al., 1997, “High-performance three-dimensional electromagnetic modelling using modified Neumann series. Wide-band numerical solution and examples”, *Journal of geomagnetism and geoelectricity*, v. 49, n. 11-12, pp. 1519–1539.
- BAHR, K., 1988, “Interpretation of the magnetotelluric impedance tensor: regional induction and local telluric distortion”, *J. Geophys.*, v. 62, n. 2, pp. 119–127.
- BELLO, M., LIU, J., GUO, R., 2019, “Three-Dimensional Wide-Band Electromagnetic Forward Modelling Using Potential Technique”, *Applied Sciences*, v. 9, n. 7, pp. 1328.
- BIBBY, H., CALDWELL, T., BROWN, C., 2005, “Determinable and non-determinable parameters of galvanic distortion in magnetotellurics”, *Geophysical Journal International*, v. 163, n. 3, pp. 915–930.
- BOSTICK, F., 1977, “A simple almost exact method of MT analysis, workshop on electrical methods in geothermal exploration”, *US Geol. Surv.*
- CAGNIARD, L., 1953, “Basic Theory of the Magnetotelluric Method of Geophysical Prospecting”, *Geophysics*, v. 18, pp. 605–635.

- CAINELLI, C., MOHRIAK, W. U., 1999, “Some remarks on the evolution of sedimentary basins along the Eastern Brazilian continental margin”, *Episodes- Newsmagazine of the International Union of Geological Sciences*, v. 22, n. 3, pp. 206–216.
- CALDWELL, T. G., BIBBY, H. M., BROWN, C., 2004, “The magnetotelluric phase tensor”, *Geophysical Journal International*, v. 158, n. 2, pp. 457–469.
- CHANG, H. K., KOWSMANN, R. O., FIGUEIREDO, A. M. F., et al., 1992, “Tectonics and stratigraphy of the East Brazil Rift system: an overview”, *Tectonophysics*, v. 213, n. 1-2, pp. 97–138.
- CHANG, H. K., ASSINE, M. L., CORRÊA, F. S., et al., 2008, “Sistemas petrolíferos e modelos de acumulação de hidrocarbonetos na Bacia de Santos”, *Revista Brasileira de Geociências*, v. 38, n. 2 suppl, pp. 29–46.
- CHAVE, A. D., CONSTABLE, S. C., EDWARDS, R. N., 1991, “Electrical exploration methods for the seafloor”. In: Nabighian, M. N. (Ed.), *Electromagnetic Methods in Applied Geophysics: Volume 2, Application, Parts A and B*, Society of Exploration Geophysicists, pp. 931–966.
- COMMER, M., NEWMAN, G. A., 2009, “Three-dimensional controlled-source electromagnetic and magnetotelluric joint inversion”, *Geophysical Journal International*, v. 178, n. 3, pp. 1305–1316.
- CONSTABLE, S. C., ORANGE, A. S., HOVERSTEN, G. M., et al., 1998, “Marine magnetotellurics for petroleum exploration Part I: A sea-floor equipment system”, *Geophysics*, v. 63, n. 3, pp. 816–825.
- DE LUGAO, P., FONTES, S., LA TERRA, E., et al., 2008, “First application of marine magnetotellurics improves depth imaging in the Santos Basin, Brazil”. In: *70th EAGE Conference and Exhibition incorporating SPE EUROPEC 2008*, June.
- DONG, H., JONES, A. G., 2018, “On the Influences of Random Starting/Prior Models in Three-Dimensional Magnetotelluric Inversion”. In: *EMIW Electromagnetic Induction Workshop Abstracts 2018*, p. 106, Helsingor, Denmark, August.
- EGBERT, G. D., BOOKER, J. R., 1986, “Robust estimation of geomagnetic transfer functions”, *Geophysical Journal International*, v. 87, n. 1, pp. 173–194.

- EGBERT, G. D., KELBERT, A., 2012, “Computational recipes for electromagnetic inverse problems”, *Geophysical Journal International*, v. 189, n. 1, pp. 251–267.
- EGBERT, G. D., MEQBEL, N., KELBERT, A., 2017, “Some results from ModEM3DMT, the freely available OSU 3D MT inversion code”, *6th International Symposium on Three-Dimensional Electromagnetics*, (March).
- FARQUHARSON, C. G., OLDENBURG, D. W., HABER, E., et al., 2002, “An algorithm for the three-dimensional inversion of magnetotelluric data”. In: *SEG Technical Program Expanded Abstracts 2002*, Society of Exploration Geophysicists, pp. 649–652.
- FILLOUX, J., 1980, “Magnetotelluric soundings over the northeast Pacific may reveal spatial dependence of depth and conductance of the asthenosphere”, *Earth and Planetary Science Letters*, v. 46, n. 2, pp. 244–252.
- FONTES, S., DE LUGAO, P., MEJU, M., et al., 2009, “Marine magnetotelluric mapping of basement and salt bodies in the Santos Basin of Brazil”, *First Break*, v. v. 27 (05), pp. p. 83–87.
- GALLARDO, L., FONTES, S., MEJU, M., et al., 2012, “Robust geophysical integration through structure-coupled joint inversion and multispectral fusion of seismic reflection, magnetotelluric, magnetic, and gravity images: Example from Santos Basin, offshore Brazil”, *Geophysics*, v. 77 (09), pp. 237–B251. doi: 10.1190/geo2011-0394.1.
- GAMBLE, T. D., GOUBAU, W. M., CLARKE, J., 1979, “Magnetotellurics with a remote magnetic reference”, *Geophysics*, v. 44, n. 1, pp. 53–68.
- GARCIA, S. F. D. M., 2012, *Restauração estrutural da halotectônica na porção central da bacia de Santos e implicações para os sistemas petrolíferos*. Tese de Doutorado, Escola de Minas, Universidade Federal de Ouro Preto.
- GROOM, R. W., BAILEY, R. C., 1989, “Decomposition of magnetotelluric impedance tensors in the presence of local three-dimensional galvanic distortion”, *Journal of Geophysical Research: Solid Earth*, v. 94, n. B2, pp. 1913–1925.
- GUERRA, M. C., UNDERHILL, J. R., 2012, “Role of halokinesis in controlling structural styles and sediment dispersal in the Santos Basin, offshore Brazil”, *Geological Society, London, Special Publications*, v. 363, n. 1, pp. 175–206.

- HOVERSTEN, G. M., CONSTABLE, S. C., MORRISON, H. F., 2000, “Marine magnetotellurics for base-of-salt mapping: Gulf of Mexico field test at the Gemini structure”, *Geophysics*, v. 65, n. 5, pp. 1476–1488.
- HURSAN, G., ZHDANOV, M. S., 2002, “Contraction integral equation method in three-dimensional electromagnetic modeling”, *Radio Science*, v. 37, n. 6, pp. 1–1.
- KELBERT, A., MEQBEL, N., EGBERT, G. D., et al., 2014, “ModEM: A modular system for inversion of electromagnetic geophysical data”, *Computers & Geosciences*, v. 66, pp. 40–53.
- KELLETT, R., LILLEY, F., WHITE, A., 1991, “A two-dimensional interpretation of the geomagnetic coast effect of southeast Australia, observed on land and seafloor”, *Tectonophysics*, v. 192, n. 3-4, pp. 367–382.
- KEY, K. W., CONSTABLE, S. C., WEISS, C. J., 2006, “Mapping 3D salt using the 2D marine magnetotelluric method: Case study from Gemini Prospect, Gulf of Mexico”, *Geophysics*, v. 71, n. 1, pp. B17–B27.
- KRIEGER, L., PEACOCK, J. R., 2014, “MTpy: A Python toolbox for magnetotellurics”, *Computers & Geosciences*, v. 72, pp. 167–175.
- KRUGLYAKOV, M., KUVSHINOV, A., 2018, “Using high-order polynomial basis in 3-D EM forward modeling based on volume integral equation method”, *Geophysical Journal International*, v. 213, n. 2, pp. 1387–1401.
- LINDSEY, N. J., NEWMAN, G. A., 2015, “Improved workflow for 3D inverse modeling of magnetotelluric data: Examples from five geothermal systems”, *Geothermics*, v. 53, pp. 527–532.
- MACKIE, R. L., MADDEN, T. R., 1993, “Three-dimensional magnetotelluric inversion using conjugate gradients”, *Geophysical Journal International*, v. 115, n. 1, pp. 215–229.
- MACKIE, R. L., MADDEN, T. R., WANNAMAKER, P. E., 1993, “Three-dimensional magnetotelluric modeling using difference equations - Theory and comparisons to integral equation solutions”, *Geophysics*, v. 58, n. 2, pp. 215–226.
- MARTI, A., QUERALT, P., LEDO, J., 2009, “WALDIM: A code for the dimensionality analysis of magnetotelluric data using the rotational invariants of the magnetotelluric tensor”, *Computers & Geosciences*, v. 35, n. 12, pp. 2295–2303.

- MATSUNO, T., SEAMA, N., EVANS, R. L., et al., 2010, “Upper mantle electrical resistivity structure beneath the central Mariana subduction system”, *Geochemistry, Geophysics, Geosystems*, v. 11, n. 9.
- MCKENZIE, D., 1978, “Some remarks on the development of sedimentary basins”, *Earth and Planetary science letters*, v. 40, n. 1, pp. 25–32.
- MEQBEL, N., WECKMANN, U., MUÑOZ, G., et al., 2016, “Crustal metamorphic fluid flux beneath the Dead Sea Basin: constraints from 2-D and 3-D magnetotelluric modelling”, *Geophysical Supplements to the Monthly Notices of the Royal Astronomical Society*, v. 207, n. 3, pp. 1609–1629.
- MEQBEL, N. M. M., 2009, *The electrical conductivity structure of the Dead Sea Basin derived from 2D and 3D inversion of magnetotelluric data*. Tese de Doutorado, Freien Universit?at Berlin.
- MIENSOPUST, M. P., 2017, “Application of 3-d electromagnetic inversion in practice: Challenges, pitfalls and solution approaches”, *Surveys in Geophysics*, v. 38, n. 5, pp. 869–933.
- MODICA, C. J., BRUSH, E. R., 2004, “Postrift sequence stratigraphy, paleogeography, and fill history of the deep-water Santos Basin, offshore southeast Brazil”, *AAPG bulletin*, v. 88, n. 7, pp. 923–945.
- MOHRIAK, W., MACEDO, J., CASTELLANI, R., et al., 1995, “Salt tectonics and structural styles in the deep-water province of the Cabo Frio region, Rio de Janeiro, Brazil”, *Salt tectonics: a global perspective*, pp. 273–304.
- MOREIRA, J. L. P., MADEIRA, C. V., GIL, J. A., et al., 2007, “Bacia de Santos”, *Boletim de Geociências da Petrobras*, v. 15, n. 2, pp. 531–549.
- NEWMAN, G. A., BOGGS, P. T., 2004, “Solution accelerators for large-scale three-dimensional electromagnetic inverse problems”, *Inverse Problems*, v. 20, n. 6, pp. S151.
- NIBLETT, E. R., SAYN-WITTGENSTEIN, C., 1960, “Variation of electrical conductivity with depth by the magneto-telluric method”, *Geophysics*, v. 25, n. 5, pp. 998–1008.
- OLDENBURG, D., 1981, “Conductivity structure of oceanic upper mantle beneath the Pacific plate”, *Geophysical Journal International*, v. 65, n. 2, pp. 359–394.

- PANETTO, L. P., LA TERRA, E. F., TUPINAMBÁ, M., et al., 2018, “Crustal framework of the Ribeira and Brasília belts (SE Brazil) inferred from 3D magnetotelluric imaging”, *Journal of South American Earth Sciences*, v. 86, pp. 342–352.
- PATRO, P. K., EGBERT, G. D., 2011, “Application of 3D inversion to magnetotelluric profile data from the Deccan Volcanic Province of Western India”, *Physics of the Earth and Planetary Interiors*, v. 187, n. 1-2, pp. 33–46.
- RAICHE, A., 1974, “An integral equation approach to three-dimensional modelling”, *Geophysical Journal International*, v. 36, n. 2, pp. 363–376.
- REDDY, I., RANKIN, D., PHILLIPS, R., 1977, “Three-dimensional modelling in magnetotelluric and magnetic variational sounding”, *Geophysical Journal International*, v. 51, n. 2, pp. 313–325.
- RIKITAKE, T., 1948, “1. Notes on the Electromagnetic Induction within the Earth”, *Earthquake Research Institute*, v. 24, pp. 1–9.
- RODI, W., MACKIE, R. L., 2001, “Nonlinear conjugate gradients algorithm for 2-D magnetotelluric inversion”, *Geophysics*, v. 66, n. 1, pp. 174–187.
- SASAKI, Y., 2004, “Three-dimensional inversion of static-shifted magnetotelluric data”, *Earth, planets and space*, v. 56, n. 2, pp. 239–248.
- SIMPSON, F., BAHR, K., 2005, *Practical magnetotellurics*. Cambridge University Press.
- SIRIPUNVARAPORN, W., 2012, “Three-dimensional magnetotelluric inversion: an introductory guide for developers and users”, *Surveys in geophysics*, v. 33, n. 1, pp. 5–27.
- SIRIPUNVARAPORN, W., EGBERT, G., 2007, “Data space conjugate gradient inversion for 2-D magnetotelluric data”, *Geophysical Journal International*, v. 170, n. 3, pp. 986–994.
- SIRIPUNVARAPORN, W., EGBERT, G., LENBURY, Y., 2002, “Numerical accuracy of magnetotelluric modeling: a comparison of finite difference approximations”, *Earth, planets and space*, v. 54, n. 6, pp. 721–725.
- SMITH, J. T., BOOKER, J. R., 1991, “Rapid inversion of two-and three-dimensional magnetotelluric data”, *Journal of Geophysical Research: Solid Earth*, v. 96, n. B3, pp. 3905–3922.

- SWIFT, C. M., 1967, *A Magnetotelluric Investigation of an Electrical Conductivity anomaly in the Southwestern United States*. Tese de Doutorado, Massachusetts Institute of Technology.
- TIKHONOV, A., 1950, “On Determining Electrical Characteristics of the Deep Strata of Earth’s Crust”, *Doklady*, v. 73, pp. 295–297.
- VOZOFF, K., 1991, “The Magnetotelluric Method”. In: Nabighian, M. N. (Ed.), *Electromagnetic Methods in Applied Geophysics: Volume 2, Application, Parts A and B*, Society of Exploration Geophysicists, pp. 641–712.
- WANNAMAKER, P. E., 1991, “Advances in three-dimensional magnetotelluric modeling using integral equations”, *Geophysics*, v. 56, n. 11, pp. 1716–1728.
- WEAVER, J. T., AGARWAL, A. K., LILLEY, F., 2000, “Characterization of the magnetotelluric tensor in terms of its invariants”, *Geophysical Journal International*, v. 141, n. 2, pp. 321–336.
- WEISS, C. J., 2013, “Project APhiD: A Lorenz-gauged $A-\Phi$ decomposition for parallelized computation of ultra-broadband electromagnetic induction in a fully heterogeneous Earth”, *Computers & geosciences*, v. 58, pp. 40–52.
- WIGHT, D. E., BOSTICK, F., SMITH, H., 1977, “Real-time Fourier transformation of magnetotelluric data”, *US Department of Energy*.
- WORD, D. R., SMITH, H. W., BOSTICK JR, F., 1970, *An Investigation of the Magnetotelluric Tensor Impedance Method*. Relatório técnico, Electronics Research Center, University of Texas at Austin.
- YEE, K., 1966, “Numerical solution of initial boundary value problems involving Maxwell’s equations in isotropic media”, *IEEE Transactions on antennas and propagation*, v. 14, n. 3, pp. 302–307.
- ZHDANOV, M. S., LEE, S. K., YOSHIOKA, K., 2006, “Integral equation method for 3D modeling of electromagnetic fields in complex structures with inhomogeneous background conductivity”, *Geophysics*, v. 71, n. 6, pp. G333–G345.

Appendix

